

Review on UAV-based FSO links: recent advances, challenges, and performance metrics

Aanchal Gupta ^{*}, Divya Dhawan, and Neena Gupta

Punjab Engineering College (Deemed to be University), Department of Electronics and Communication Engineering, Chandigarh, India

ABSTRACT. With the rapid advancements in wireless technology, the incorporation of unmanned aerial vehicles (UAVs) in free space optical (FSO) communication can reap several benefits related to coverage, security, and capacity. The parameters involved for the analysis of such systems are studied in detail. The irradiance fluctuations in the received beam due to turbulence induced fading and geometric and misalignment effects are to be taken care of in order to minimize the bit error rate. The random variables involved in a UAV-employed FSO link are larger than that present in an FSO system. Thus, efficient designing of a UAV-employed FSO system is relatively more challenging as compared to a ground-based terrestrial FSO link. There are many performance metrics that can be defined and are to be analyzed in order to optimize the parameters associated with UAV-based FSO systems and design a link with good quality of service. Some recent methods are also explored for further improving the reliability and coverage of UAV based FSO networks.

© 2023 Society of Photo-Optical Instrumentation Engineers (SPIE) [DOI: [10.1117/1.OE.63.4.041204](https://doi.org/10.1117/1.OE.63.4.041204)]

Keywords: unmanned aerial vehicle; free space optics; atmospheric loss; turbulence induced fading; pointing errors; angle of arrival fluctuations

Paper 20230595SSV received Jun. 22, 2023; revised Sep. 13, 2023; accepted Sep. 27, 2023; published Oct. 18, 2023.

1 Introduction

Due to the ever growing demand of high capacity in the field of wireless communication, free space optical (FSO)¹⁻⁴ communication is gaining more and more attention of the researchers. The increasing congestion of the electromagnetic spectrum and the growing risk of eavesdropping attacks make FSO a promising alternative to radio communication. FSO communication offers many advantages over the conventional radio frequency (RF) communication, such as it provides inherently secure communication, huge capacity (upto 2.5 Gbps), license-free spectrum, cost effective solution, and low power consumption.^{5,6} Owing to the broadcast nature of radio communication, it is still considered as first choice in many situations especially in vehicular and mobile communication, where the source or destination is moving. The multiple benefits of FSO communication make it a suitable candidate for upcoming 6G communication, which requires very fast data transfer rate, ultra low latency, greater support for M2M (machine-to-machine) connections, and higher network reliability.^{7,8} FSO has many attractive applications, such as inter-building connectivity, video surveillance, video broadcasting, disaster management, and backhauling for cellular networks.^{3,5} It has also paved its way in space applications including satellite communication and remote sensing.⁹ FSO technology also has a major drawback, which is the requirement of a line-of-sight (LoS) between the transmitter and the receiver, which mainly depends on their misalignment. FSO transceivers should be perfectly facing each other in order to transfer the information. Unmanned aerial vehicles (UAVs), such as multi-rotor drones, low-

*Address all correspondence to Aanchal Gupta, aanchalgupta.phd22ece@pec.edu.in

altitude, or high-altitude balloons, serve as a boon for carrying out communication in disaster-struck areas, such as in cases of natural calamities, floods, and earthquakes, when ground based terrestrial communication comes to a halt and only aerial communication is possible.^{10,11} Owing to the in-built feature of aerial communication of providing higher chances of LoS communication, using FSO to connect aerial nodes has huge scope for future communication systems.¹²⁻¹⁴ Recent developments in UAVs and FSO communication have offered new benchmarks in designing UAV based FSO links.¹⁵ UAVs also find applications in matters related to national security, aerial photography, accident investigation, and in situations where LoS communication is not possible due to the presence of tall buildings or because of the huge crowd. UAVs help increase the coverage area and also offer dynamic deployment, low cost, and low power requirement. Therefore, UAV as an information relay is a hot topic of research in prevailing scenario.

A UAV-based FSO system is subjected to various challenges. An optical signal is vulnerable to many impairments that degrade the performance of the system.¹⁶ Attenuation due to rain, fog, dust particles, haze and snow, turbulence-induced fading mainly due to scintillation,^{17,18} pointing errors because of the misalignment,^{19,20} and angle-of-arrival (AoA) fluctuations are the major causes of signal degradation while propagating through the atmosphere. Out of the four channel deterioration effects, atmospheric loss is assumed to be deterministic and remaining three are considered as independent random events. These phenomena give rise to irradiance fluctuations in the beam intensity and lead to low reliability and low quality of service. Pointing errors include the position deviations of the transmitter and receiver and orientation fluctuations of the hovering UAV. Position deviations can occur because of the building sway, thermal expansion, and strong windy weather. AoA fluctuations are caused when the incoming optical beam is no longer perpendicular to the detector plane. A combination of AoA fluctuations and pointing errors is known as geometric misalignment loss (GML).

In this brief, a detailed study of all the key channel impairments in FSO systems is presented. Various turbulence models for representing different turbulence conditions are demonstrated. Here, main focus is given on the analytical channel modeling of the radial displacement caused due to pointing errors and link interruption due to AoA fluctuations. The case of non-zero bore-sight error is also considered along with discussion on angles of arrival for different link configurations including U2G, G2U, and U2U links. In UAV-based FSO links, all these random variations play a major role in determining the link quality and neither of them can be ignored during the analysis. In addition to all this, the paper depicts various applications and contributions of UAVs and shares information about the work done in the field of FSO, specifically related to the measurement of several link metrics. Various geometric loss models introduced in the literature for meeting specific link requirements or for realizing a real-life scenario are also discussed in this brief. Latest techniques that can contribute toward the performance improvement of UAV and FSO based networks are also explained. To the best of my knowledge, this type of extensive review on UAV-employed FSO links is not presented before in the literature. The remaining paper is set as follows: Secs. 2 and 3 are devoted to a brief introduction of FSO networks and UAV communication, Sec. 4 gives a description about the modeling of all the channel degradation effects involved along with an introduction of the geometric loss models currently used in the literature, and Sec. 5 defines and analyzes various performance metrics for a UAV-based FSO link for optimizing the system parameters. Section 6 gives an overview of the latest techniques employed with UAV based FSO networks.

2 Overview of FSO

FSO or fiberless photonics is an LoS technology in which a narrow optical beam is transmitted through free space toward the receiver.²¹ FSO serves as a promising solution to the last mile issue between the optical fiber infrastructure and destination users. It is extensively utilized in several areas, especially where optical fiber installation is a hard nut to crack. As in any wireless communication system, FSO also has a transmitter, a receiver, and free space channel. At the transmitting end, the electrical signal is converted to an optical signal using the principle of electroluminescence and at the receiver side, the received laser beam is converted back into electrical form through the principle of absorption or photo-detection. Figure 1 shows the basic block diagram of an FSO communication system. The transmitter mainly comprises of a light source,

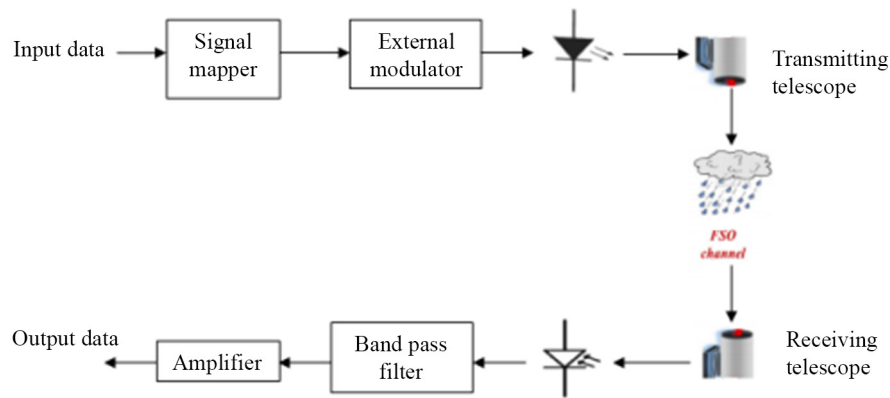


Fig. 1 Block diagram of an FSO communication system.

an external modulator, and a transmitting telescope. Light source used can be either a light emitting diode (LED) or a laser diode (LD). Due to the monochromatic and coherent properties of light emitted from a laser, laser is preferred for most of the applications. A driver circuit is used to vary the flow of current through the laser. Light modulation can be done in two ways, either using direct modulation or by using an external modulator. In direct modulation, digital bit stream is directly converted into an analog optical signal inside laser whereas, in external modulation, modulation is done outside the laser resonator. The most commonly used external modulator is Mach–Zehnder modulator. The receiver consists of following components: a receiving telescope, detector, amplifier, and filter. The transmitting telescope collimates the optical beam²² and focuses it toward the photo-detector, whereas, the receiving telescope collects the incoming beam. Photo-detector used can be either a P-I-N photo-diode or an avalanche photo-diode (APD). For high quantum efficiency, APD is preferred but its drawback is that it adds more noise to the signal as compared to a P-I-N photo-diode. Aperture averaging must be performed in order to combine the multiple uncorrelated signals and focus the averaged signal to the photo-detector, and optical filtering is done to filter out all the unwanted wavelengths and background solar illumination.

3 Significant Contributions of UAV

UAVs have drawn considerable attention of researchers due to their wide applications in military, surveillance, disaster management, traffic management, wireless networks, etc.^{11,13,23} They offer a flexible, low cost solution for providing controllable mobility in order to carry out wireless communication. As and when required, they can be deployed on demand easily. UAVs form a great combination with FSO communication as they are aerial devices and their location can always be altered to offer an LoS path between the transceivers. They can be made to function as base stations, relays, and cooperative jamming devices. Figure 2 demonstrates the various functionalities of UAVs. Owing to the miniaturization, compactness, and light-weight of detecting optical devices, UAVs are also explored to a great extent as eavesdroppers. UAVs, functioning as relays, can provide large coverage and thus, huge wireless connectivity. They can work as friendly jammers and send jamming signals in order to confuse the eavesdroppers, resulting in more secured communication. Optimal values of the parameters, such as UAV jammer's location and its transmit power, can be obtained by maximizing the secrecy rate. The integration of UAVs with reconfigurable optical reflecting intelligent surfaces (RORIS)^{24–26} is also gaining attention of researchers as it further helps in improving the coverage and spectral efficiency.

FSO communication is prone to eavesdropping attacks. This is because the beam diameter increases with the transmission distance, and it becomes wider than the receiver aperture. For a beam divergence angle of 1 mrad, the beam diameter for a 10 km link becomes 10 m.²⁷ Because of the rapid miniaturization and light weight of optical devices, it is possible for UAVs to eavesdrop in FSO links. Thus, the wireless optical networks are at high tapping risks and part of their radiated power can be captured by the eavesdropper. Therefore, security is of critical importance

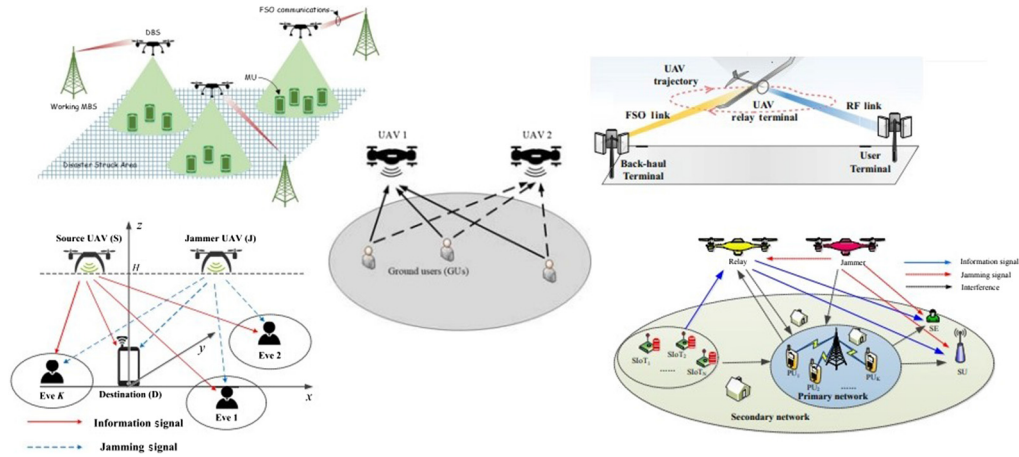


Fig. 2 Various applications of UAV.

in UAV based FSO communications systems owing to the vast applications of UAVs in military, defence, and other government related organizations. One major challenge encountered with UAVs is their limited battery life.²⁸ The energy consumption in a UAV happens due to two reasons: first because of the involvement in communication and second (dominant factor) is because of the propulsion energy of UAV, which is consumed due to hovering of UAV. Thus, while designing a UAV based FSO link, security requirements, battery limitation, and other such factors have to be kept in mind.

Due to the ever-increasing demand of flying autonomous vehicles, researchers are coming up with many innovative ideas in order to utilize UAVs to the maximum extent. Considering several models according to specific UAV application, applying different optimization algorithms, and using various metrics for optimizing overall system performance, all contribute toward effective and novel UAV related research ideas. Different cooperative relaying techniques can be applied at the UAV, such as decode and forward and amplify and forward, for obtaining improved system reliability. Other latest technologies, such as cognitive radio (CR),²⁹ millimeter wave (mmWave) communication,³⁰ non-orthogonal multiple access (NOMA)^{31,32} etc., can be further incorporated in UAV-based networks in order to exploit various advantages, such as improved throughput, better spectrum utilization and spectral efficiency, and low latency. A summary of various UAV-based applications is demonstrated in Table 1.

Table 1 Summary of UAV based applications.

Reference	Action	Technique used	Objective
23	Relay	QoS aware drone base station placement and mobile user association strategy (RESCUE)	Maximize the mobile users (MUs) served in a disaster-struck area
33	Relay	Transmission schemes according to the delay requirements, delay-limited transmission, and delay-tolerant transmission	Maximize throughput in mixed RF/FSO networks
34	Relay	Amplify and forward relaying	Minimize outage probability
35	Relay	Decode and forward relaying	Minimize outage probability
27	Eavesdropper	Three eavesdropping scenarios: (1) Eve is between Alice and Bob, (2) Eve and Bob are in the same receiving plane, and (3) Eve is behind Bob	Analyze SOP

Table 1 (Continued).

Reference	Action	Technique used	Objective
36	Relay	UAVs as buffer-aided and non-buffer-aided relays	Analyze ergodic sum rate
37	Relay	Decode and forward relaying	Derive a tractable statistical channel model along with link outage and end-to-end outage probability
38	Jammer	Three random deployment processes as UAV's location is unknown	Achieve optimal secrecy rate
30	Relay	Millimeter wave (mmWave)	Derive tractable channel models for three UAV communication scenarios
39	Relay and jammer	Vectorization method	Mitigate interception and increase secrecy rate
40	Jammer	An alternating iterative algorithm and successive convex approximation technique	Maximize the minimum average secrecy rate
41	Jammer	Matern hardcore point process and transmit jamming strategy	Improve secrecy performance
42	Relay	Decode and forward relaying	Analyze intercept probability and ergodic secrecy rate
43	Jammer	Adaptive secrecy transmission policy based on the Wyner encoding scheme and block coordinate descent method	Maximize the secrecy energy efficiency
44	Relay	Security-on-demand UAV and non-security-on-demand UAV	Maximize achievable secrecy rate
45	Relay and jammer	Successive convex approximation technology and alternate optimization method	Maximize average worst-case secrecy rate
25	Relay	Reconfigurable optical intelligent reflecting surface	Derive overall outage probability and average BER
29	Relay and secondary transmitter	CR	Maximize the total secrecy rate
46	Relay	Two UAV selection strategies, best harmonic mean, and best downlink SNR	Examine end-to-end outage probability, coverage probability, and throughput
47	Jammer	Block coordinate descent and successive convex optimization method	Maximize worst-case secrecy rate
48	Relay	Alternating optimization approach	Maximize secrecy rate
49	Relay	Successive convex optimization method	Maximize average worst-case secrecy rate
32	Base station	NOMA	Maximize the minimum secrecy rate of MUs
50	Base station	Cooperative rate-splitting and sequential parametric convex approximation method	Investigate max-min secrecy

4 Channel Impairments in UAV Based FSO Systems

4.1 Atmospheric Loss

Attenuation of the optical signal (also known as atmospheric loss) is related to visibility and it varies with time. This loss is caused due to the scattering and absorption of the optical beam. Absorption loss refers to the reduction in signal energy due to the absorption by particles (molecules or aerosols) present in the atmosphere. Scattering occurs when the light redistributes after colliding with the particles present in the medium. Scattering and absorption both are wavelength dependent phenomena. Scattering can be Rayleigh, Mie, or non-selective depending upon the size of the particle and the wavelength of the optical beam. Atmospheric attenuation is modeled by Beer Lambert's law as²⁷

$$h_a = \Delta \exp(-\alpha_v Z), \quad (1)$$

where $\Delta = \frac{(2a)^2}{(2w_z)^2}$, a is the receiver aperture radius, w_z is the beamwidth, Z is the propagation distance (in km), and α_v is the atmospheric attenuation factor measured in dB/km. Assuming the Mie scattering model, the value of α_v is given as³

$$\alpha_v = \frac{3.91}{V} \left(\frac{\lambda}{550 \text{ nm}} \right)^{-\delta}, \quad (2)$$

where V is the visibility range in km, 550 nm is the visibility range reference wavelength, λ is the wavelength of operation in nm, and δ is the coefficient of scattering related to size distribution. The value of this scattering coefficient can be determined by either using the Kim model or Kruse model.³ For large attenuation, Kim model is preferred. As per Kruse model

$$\delta = \begin{cases} 1.6, & V > 50 \\ 1.3, & 6 < V < 50. \\ 0.585V^{1/3}, & V < 6 \end{cases} \quad (3)$$

As per Kim model

$$\delta = \begin{cases} 1.6, & V > 50 \\ 1.3, & 6 < V < 50 \\ 0.16V + 0.34, & 1 < V < 6 \\ V - 0.5, & 0.5 < V < 1 \\ 0, & V < 0.5 \end{cases} \quad (4)$$

4.2 Turbulence-Induced Fading

The atmosphere can be assumed to have two different states: laminar flow and turbulent flow.² In the first one, the characteristics of velocity are uniform, and they do not change in a random manner while in the latter case, due to dynamic mixing, the velocity possesses random characteristics and incorporates random sub-flows called turbulent eddies. These eddies cause the light beam to deflect from its transmission path. The formation of these turbulent eddies is because of the temperature and pressure variation of air. This variation (mainly temperature fluctuations) ultimately leads to a variation in the refractive index of atmosphere, which is depicted through a parameter known as refractive index structure parameter, C_n^2 . Depending upon the turbulent eddy size and the transmitter beam size, three types of turbulence effects can be noticed:²

- Beam wander:** If the size of the eddies is larger than the transmitter beam size, this completely deflects the beam from its path in a random fashion.⁵¹ This can result in the beam missing the receiver plane due to pointing error displacement.
- Beam scintillation:** If the size of the turbulent eddies is comparable to the transmitter beam size, eddies start behaving as lenses, which results in continuous focusing and de-focusing of the incoming beam. This is the most common turbulence effect, and it results in irradiance fluctuations and fading of the received beam.^{52,53} This scintillation effect is measured in terms of scintillation index (also known as the normalized variance of irradiance, σ_I^2). Rytov variance, σ_R^2 , also called variance of log irradiance, is a convenient parameter denoting the strength of scintillation, and it is given as⁵⁴

Table 2 Rytov variance for different turbulence loads.

Range	Turbulence
$\sigma_R^2 \leq 0.5$	Weak
$0.5 < \sigma_R^2 \leq 5$	Medium to strong
$5 < \sigma_R^2 \leq 25$	Strong to saturation

$$\sigma_R^2 = 1.23C_n^2 K^{7/6} Z^{11/6}, \quad (5)$$

where K is the free space wave number given by $2\pi/\lambda$. C_n^2 can have an average value from $10^{-17} \text{ m}^{-2/3}$ to $10^{-13} \text{ m}^{-2/3}$ for weak to strong turbulence channels.² Rytov variation for different turbulence conditions is shown in Table 2.

- (c) **Beam spreading:** If the size of eddy is smaller than the beam size, then the beam is diffracted near the aperture of the receiver.⁵¹ This results in reduction of the received power density and distortion of the beam wavefront. Beam spreading can be reduced by increasing the aperture area.

4.2.1 Probability density functions for modeling turbulence

There are various channel models for characterizing different weather conditions and effects of atmospheric turbulence.⁵⁵ For determining the effect of turbulence induced fading on the performance of UAV-based FSO systems, many statistical channel models have been considered in the literature. The expressions for the probability density functions (PDFs) for different scenarios along with the pros and cons of each of them are explained in subsequent detail.

- (i) **Log-normal distribution (for weak to moderate turbulence):** For weak turbulence conditions, log-normal fading model is employed to describe the turbulence effect on the strength of the optical beam. Its PDF is given as⁵⁶

$$f_{h_t}(h_t) = \frac{1}{2h_t\sqrt{2\pi\sigma_x^2}} \exp\left(-\frac{(\ln h_t + 2\sigma_x^2)^2}{8\sigma_x^2}\right), \quad (6)$$

where σ_x^2 is the log-amplitude variance, which is related to the Rytov variance as $\sigma_x^2 = \sigma_R^2/4 = 0.31k^{7/6}C_n^2D^{11/6}$. The parameters for this model can be directly measured for UAV-based FSO systems.

- (ii) **Gamma-Gamma distribution (for moderate to strong turbulence):** For characterizing moderate to strong turbulence conditions, Gamma-Gamma model has proved to be an effective solution for FSO based systems. In this case, the PDF of random variable, h_t , is given as⁵⁶

$$f_{h_t}(h_t) = \frac{2(\alpha\beta)^{\frac{\alpha+\beta}{2}}}{\Gamma(\alpha)\Gamma(\beta)} h_t^{\frac{\alpha+\beta}{2}-1} k_{\alpha-\beta}\left(2\sqrt{\alpha\beta}h_t\right), \quad (7)$$

where $\Gamma(\cdot)$ is the Gamma function and $k_{\alpha-\beta}$ is the modified bessel function of second kind of order $\alpha - \beta$. The parameters α and β are numbers denoting the large scale and small scale eddies, and they are defined as (for the case of plane waves):³⁷

$$\alpha = \left[\exp\left(\frac{0.49\sigma_R^2}{(1 + 1.11\sigma_R^{12/5})^{7/6}}\right) - 1 \right]^{-1}, \quad (8)$$

$$\beta = \left[\exp\left(\frac{0.51\sigma_R^2}{(1 + 0.69\sigma_R^{12/5})^{5/6}}\right) - 1 \right]^{-1}. \quad (9)$$

- (iii) **Malaga (\mathcal{M}) distribution:** In order to model the turbulence induced fading, generalized \mathcal{M} distribution^{57,58} is also widely used as it is a unified model that can be used to implement all other statistical distributions and is valid for all turbulence regimes. This distribution relies

Table 3 Parameters of \mathcal{M} distribution.

Symbol	Description
Ω	Power of LoS component
Ω'	Power of both LoS and coupled to LoS components
ϕ_l	LoS component's phase
ϕ_c	Coupled-to-LoS component's phase
g	Power of NLoS off-axis scatter component
$0 < \rho < 1$	Fraction of scattering power coupled to LoS component

on double stochastic scintillation concept that allows the irradiance fluctuations to be modeled as the product of two independent random variables. Large scale turbulence effects or eddies represent the refractive effects, and small scale eddies represent the diffractive effects. \mathcal{M} distribution categorizes small scale fading into three components:⁵⁹ a coherent LoS component, a scattered coupled-to-LoS component introduced by the on-axis eddies, and a second scattered non line of sight (NLoS) component generated by the off-axis eddies. This NLoS component is totally independent of the other two. The PDF of \mathcal{M} random variable is given as⁶⁰

$$f_{h_t}(h_t) = A_M \sum_{m=1}^{\beta} a_m h_t^{\frac{\alpha+m}{2}-1} k_{\alpha-m} \left(2\sqrt{\frac{\alpha\beta h_t}{g\beta + \Omega'}} \right), \quad (10)$$

where $A_M = \frac{2\alpha^{\alpha/2}}{g^{1+\alpha/2}\Gamma(\alpha)} \left(\frac{g\beta}{g\beta + \Omega'}\right)^{\beta+\alpha/2}$ and $a_m = (\beta-1 C_{m-1}) \frac{(g\beta + \Omega')^{1-m/2}}{(m-1)!} \left(\frac{\Omega'}{g}\right)^{m-1} \left(\frac{\alpha}{\beta}\right)^{m/2}$.

Remaining parameters are explained in Table 3.

This distribution is quite effective as it offers closed-form expressions and tractable solutions for modeling the optical irradiance fluctuations in the unbounded plane or spherical optical wavefront. Gamma–Gamma distribution and log-normal distribution are just particular cases of \mathcal{M} distribution. By setting Malaga parameters as: $\rho = 1$, $\Omega' = 1$, and $g = 0$, Gamma–Gamma model can be obtained. Similarly, log-normal distribution can be achieved by setting, $\rho = 0$ and $g \rightarrow 0$.

\mathcal{M} distribution can also be written in the form of sum of generalized- K distributions weighted by binomial coefficients.⁶¹ The coefficients of these generalized- K distributions are given by the parameters of \mathcal{M} distribution. The advantages offered by this modified model are: first it provides a simplified analytical closed form scintillation fading representation by giving a finite summation even for real values of β , second it provides a novel insight into the distribution of optical power among different sub-channels and also the probability of the signal traveling via a particular sub-channel. In order to express Eq. (10) in terms of generalized- K distribution, for $\beta \in \mathcal{N}$, the following comparison can be done:

$$h_t^{\frac{\alpha+m}{2}-1} K_{\alpha-m} \left(2\sqrt{\frac{\alpha\beta h_t}{g\beta + \Omega'}} \right) = \frac{\Gamma(\alpha)\Gamma(m)}{2} \left(\frac{g\beta + \Omega'}{\alpha\beta}\right)^{\frac{\alpha+m}{2}} K_G(h_t; \alpha, m, \mathcal{I}_m). \quad (11)$$

The PDF as per this model can be expressed as

$$f_{h_t}(h_t) = \sum_{m=1}^{\beta} k_m^{(\mathcal{N})} K_G(h_t; \alpha, m, \mathcal{I}_m), \quad (12)$$

\mathcal{I}_m , which is the irradiance of the m 'th generalized sub-channel, is given by: $\frac{m}{\beta} (g\beta + \Omega')$ and the binomial coefficients are given as

$$k_m^{(\mathcal{N})} = (\beta-1 C_{m-1}) p^{m-1} (1-p)^{\beta-m}. \quad (13)$$

Here, p is the probability of optical power coupling to the LoS component and it can be defined as

$$p = \left[1 + \left(\frac{1}{\beta} \frac{\Omega'}{g} \right)^{-1} \right]^{-1}. \quad (14)$$

For $\beta \in \mathcal{R}$, the following comparison can be done:

$$h_t^{\frac{\alpha+m}{2}-1} K_{\alpha-m} \left(2\sqrt{\frac{\alpha h_t}{g}} \right) = \frac{\Gamma(\alpha)\Gamma(m)}{2} \left(\frac{g}{\alpha} \right)^{\frac{\alpha+m}{2}} K_G(h_t; \alpha, m, \mathcal{I}_m). \quad (15)$$

Here, the PDF can be expressed as

$$f_{h_t}(h_t) = \sum_{m=1}^{\infty} k_m^{(\mathcal{R})} K_G(h_t; \alpha, m, \mathcal{I}_m). \quad (16)$$

The irradiance, in this case is given by: $\mathcal{I}_m = mg$ and the binomial coefficients can be expressed as

$$k_m^{(\mathcal{R})} = \frac{\Gamma(m-1+\beta)}{\Gamma(m)\Gamma(\beta)} p^{m-1} (1-p)^\beta. \quad (17)$$

As per the simulation results obtained for the PDFs as a function of normalized irradiance, the analytical and numerical \mathcal{M} PDFs are found to be perfectly in sync with each other.

4.3 Pointing Errors

In terrestrial FSO communication systems, transceivers are mostly installed on top of tall buildings in order to ensure an LoS. Thus, building sway, thermal expansion, building vibration, or wind loads can cause pointing errors. This error can severely limit the system reliability and degrade the performance of the link. The mean position and orientation of the aerial nodes are altered because of the various random events associated with hovering UAVs. In an optical link, the beamwidth increases with the propagation distance, i.e., the beam spreads as it travels. Thus, Gaussian profile is a good approximation to represent such a beam. Figure 3 shows the displacement between the Gaussian beam and the receiver aperture having radius, a . If the instantaneous radial displacement between the beam center and the center of the circular receiver is denoted by r_d , then the fraction of collected optical power at the detector can be given as⁶²

$$h_p \approx A_0 \exp\left(-\frac{2r_d^2}{w_{\text{eq}}^2}\right), \quad (18)$$

where A_0 represents the fraction of the power collected when the radial displacement is zero, i.e., when there is no pointing error and w_{eq} is the equivalent beamwidth, $A_0 = [\text{erf}(\nu)]^2$,

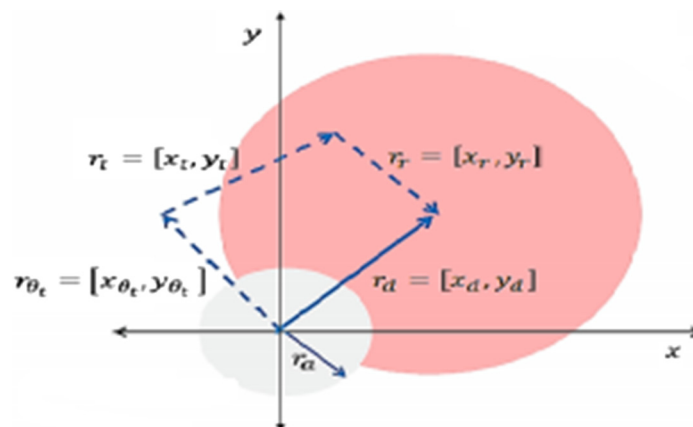


Fig. 3 Depiction of Gaussian beam footprint and receiver lens.⁶⁰

$w_{eq}^2 = w_z^2 \frac{\sqrt{\pi} \operatorname{erf}(\nu)}{2\nu \exp(-\nu^2)}$. Here, ν is the ratio of aperture radius to beamwidth, given as $\nu = \sqrt{\frac{\pi}{2}} \frac{a}{w_z}$, $\operatorname{erf}(x) = \frac{2}{\sqrt{\pi}} \int_0^x e^{-t^2} dt$ is the error function, and w_z is the Gaussian beam-waist given as⁶³

$$w_z = w_0 \sqrt{1 + \varphi \left(\frac{\lambda Z}{\pi w_0^2} \right)^2}, \tag{19}$$

where Z is the transceiver separation, w_0 is the beamwidth at $Z = 0$, and the value of φ is obtained as⁶⁰

$$\varphi = \left(1 + \frac{2w_0^2}{\rho^2(Z)} \right). \tag{20}$$

Here, $\rho(Z) = 0.55 C_n^2 K^2 Z^{-3/5}$ denotes the coherence length. For the approximation of Eq. (18) to hold, the ratio, w_z/a , should be greater than the value, 6,⁶² that is valid for most terrestrial FSO systems. Pointing errors have two components: boresight and jitter. Boresight is the mean displacement between the beam center and the center of the receiver, which occur mostly because of thermal expansion, whereas, jitter is the random beam displacement at the detector mainly because of building sway and vibrations and hovering feature of UAVs. Boresight errors severely degrade the FSO link performance. The boresight error, as reported in the literature, can be as high as 0.3 mrad.⁶² The maximum value of standard deviation of jitter for a terrestrial FSO link should be below 0.3 mrad.⁶² Pointing errors result in radial displacement between the beam center and the center of the detector, which is represented as a vector, $r_d = [x_d, y_d]$, and it comprises of three error components:

- (i) Displacement caused by the position deviation of the transmitter, $[x_t, y_t]$
- (ii) Displacement caused by the position deviation of the receiver, $[x_r, y_r]$
- (iii) Displacement caused by the transmitter UAV's orientation fluctuations, $[x_{\theta_t}, y_{\theta_t}]$

These displacements in x - z plane are shown in Fig. 4. Hence, the total displacement in y and x directions can be represented as

$$y_d = y_t + y_r + y_{\theta_t}, \quad x_d = x_t + x_r + x_{\theta_t}. \tag{21}$$

According to central limit theorem, all the above position and orientation deviations follow Gaussian distribution as they are the result of various random events. Thus, the random variables, $x_t, y_t, x_r,$ and y_r , are zero-mean Gaussian denoted as $\mathcal{N}(0, \sigma_{x_t}^2), \mathcal{N}(0, \sigma_{y_t}^2), \mathcal{N}(0, \sigma_{x_r}^2),$ and $\mathcal{N}(0, \sigma_{y_r}^2)$. Here, $\sigma_{x_t}^2$ and $\sigma_{y_t}^2$ are the variances of the transmitter's (ground/UAV) position deviation in x and y directions. Similarly, $\sigma_{x_r}^2$ and $\sigma_{y_r}^2$ are the variances of the receiver's (ground/UAV) position deviation in x and y directions, respectively. If θ_{tx} and θ_{ty} represent the bias angles of the transmitter UAV in x - z and y - z planes, then $x_{\theta_t} = Z \tan(\theta_{tx})$ and $y_{\theta_t} = Z \tan(\theta_{ty})$. As these bias angles are very small, so $x_{\theta_t} \approx Z\theta_{tx}$ and $y_{\theta_t} \approx Z\theta_{ty}$. In general, transceivers are installed with almost zero boresight error but because of the wind loads and thermal expansion, non-zero boresight exists in UAV-employed FSO links.⁶⁵ Thus, θ_{tx} ,

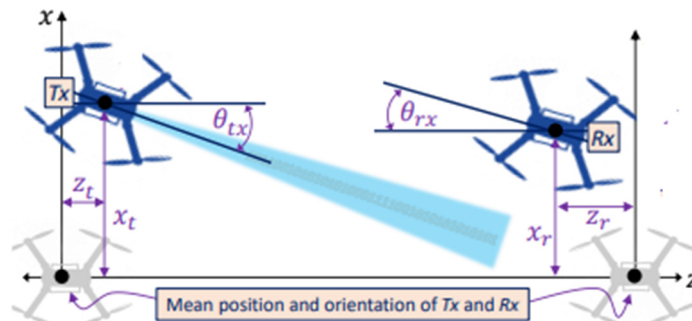


Fig. 4 Schematic of two hovering UAVs in x - z direction.⁶⁴

Table 4 Pointing error variances for different links.

Link type	Displacement variance, σ_m^2
G2U	$\sigma_{x_t}^2 + \sigma_{x_r}^2 + \sigma_{y_t}^2 + \sigma_{y_r}^2$
U2G and U2U	$\left(\frac{3Z^2\mu_{tx}^2\sigma_{dx}^4 + 3Z^2\mu_{ty}^2\sigma_{dy}^4 + \sigma_{dx}^6 + \sigma_{dy}^6}{2}\right)^{1/3}$

θ_{ty} , θ_{rx} , and θ_{ry} denote the transmitter and receiver UAV bias angles in x and y directions. Due to the numerous random events involved, these angles are assumed to be Gaussian distributed with means, μ_{tx} , μ_{ty} , μ_{rx} , μ_{ry} and variances, σ_{tx}^2 , σ_{ty}^2 , σ_{rx}^2 , and σ_{ry}^2 , respectively. For zero boresight case, $\mu_{tx} = \mu_{ty} = \mu_{rx} = \mu_{ry} = 0$. As the sum of two more Gaussian random variables is also Gaussian, the components of the radial displacement vector can thus be approximated as: $x_d \approx \mathcal{N}(Z\mu_{tx}, \sigma_{x_t}^2 + \sigma_{x_r}^2 + Z^2\sigma_{tx}^2)$ and $y_d \approx \mathcal{N}(Z\mu_{ty}, \sigma_{y_t}^2 + \sigma_{y_r}^2 + Z^2\sigma_{ty}^2)$. Then, the radial displacement, $r_d = \sqrt{x_d^2 + y_d^2}$, follows Beckmann distribution⁶⁶ also known as log-normal Rician distribution, given as

$$f_{r_d}(r_d) = \frac{r_d}{2\pi\sigma_{dx}\sigma_{dy}} \times \int_0^{2\pi} \exp\left(-\frac{(r_d \cos \phi - \mu_{tx})^2}{2\sigma_{dx}^2} - \frac{(r_d \sin \phi - \mu_{ty})^2}{2\sigma_{dy}^2}\right) d\phi. \quad (22)$$

For the case when jitter variances in x - z and y - z planes are the same, this pdf reduces to Rician distribution^{58,62} given as

$$f_{r_d}(r_d) = \frac{r_d}{\sigma_d^2} \exp\left(-\frac{(r_d^2 + \mu^2)}{2\sigma_d^2}\right) I_0\left(\frac{r_d\mu}{\sigma_d^2}\right), \quad (23)$$

where $\mu = \sqrt{\mu_{tx}^2 + \mu_{ty}^2}$ is the boresight displacement and $\sigma_d^2 = \sigma_{dx}^2 = \sigma_{dy}^2$. If the boresight displacement, $\mu = 0$, then the pdf further reduces to Rayleigh distribution. Beckmann distribution is a useful distribution but it is not in closed form. Therefore, a general Beckmann distribution approximation is used, known as modified Rayleigh distribution given as⁶⁰

$$f_{r_d}(r_d) \approx \frac{r_d}{\sigma_m^2} \exp\left(\frac{-r_d^2}{2\sigma_m^2}\right), \quad r_d \geq 0, \quad (24)$$

where the total displacement variance, σ_m^2 , for different scenarios is given in Table 4. Here, $\sigma_{dx}^2 = \sigma_{xt}^2 + \sigma_{xr}^2 + Z^2\sigma_{tx}^2$ and $\sigma_{dy}^2 = \sigma_{yt}^2 + \sigma_{yr}^2 + Z^2\sigma_{ty}^2$ denote the variances in x - z and y - z planes. On combining Eqs. (18) and (24), the overall PDF of the fluctuations caused due to pointing errors can be given as⁶⁷

$$f_{h_p}(h_p) = \frac{\zeta^2}{A_f^{\zeta^2}} h_p^{\zeta^2-1}, \quad 0 \leq h_p \leq A_0, \quad (25)$$

where $\zeta = \frac{w_{eq}}{2\sigma_m}$, i.e., the ratio of equivalent beamwidth and displacement variance and $A_f = A_0G$. Here, $G = \exp\left(\frac{1}{\zeta^2} - \frac{1}{2\zeta_x^2} - \frac{1}{2\zeta_y^2} - \frac{\mu_{tx}^2}{2\zeta_x^2\sigma_{dx}^2} - \frac{\mu_{ty}^2}{2\zeta_y^2\sigma_{dy}^2}\right)$, where $\zeta_x = \frac{w_{eq}}{2\sigma_{dx}}$ and $\zeta_y = \frac{w_{eq}}{2\sigma_{dy}}$.

4.4 Link Interruption due to AoA Fluctuations

Unlike ground terrestrial FSO links, in the presence of UAVs, the link gets interrupted because of AoA fluctuations. Due to the orientation deviations caused by UAVs at the transmitting and receiving ends, this irradiance because of AoA occurs. Due to these AoA fluctuations, the incoming beam becomes non-orthogonal to the detector plane. Building sway, experienced by the transceivers installed on top of the tall buildings and UAV's instability, results in two types of impairments: one is the pointing error that causes misalignment of the center of the beam and the receiver aperture and second is the link interruption because of AoA fluctuations that occur when the angle of arrival exceeds the receiver's field of view, represented by θ_{FoV} . In FSO systems, the incoming light is focused through a converging lens at the photo-detector but because of the orientation deviations of the hovering UAV, the received optical beam changes

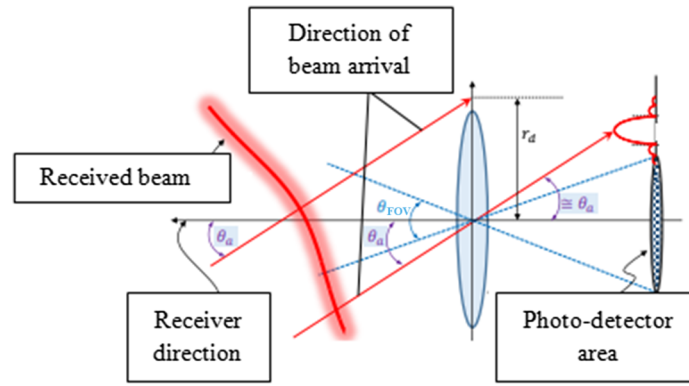


Fig. 5 AoA and field of view demonstration depicting the air pattern.³⁷

Table 5 AoA for different link configurations.

Type of link	AoA
G2U	$\sqrt{\theta_{rx}^2 + \theta_{ry}^2}$
U2G	$\sqrt{\theta_{tx}^2 + \theta_{ty}^2}$
U2U	$\sqrt{(\theta_{tx} + \theta_{rx})^2 + (\theta_{ty} + \theta_{ry})^2}$

its path and results in an airy pattern that is outside the range of the detector as shown in Fig. 5. The angles of arrival for different types of links are given in Table 5, and these different link configurations are shown in Fig. 6. In order to model this type of degradation, the channel coefficient, h_o , is defined such that it will take the value “1” if the received signal’s AoA falls inside the receiver’s field of view, that is the case when maximum power is captured otherwise it will take the value “0” as no signal is detected:

$$h_o = \begin{cases} 1, & \theta_a \leq \theta_{FOV} \\ 0, & \theta_a > \theta_{FOV} \end{cases}, \quad (26)$$

where θ_a denotes the angle of arrival of the beam at the detector plane. The channel coefficient, h_o , can be simply defined as above due to the fact that the main lobe width of the airy pattern is approximately equal to 2.4λ ³⁷ that is very small as compared to the detector size, which is in the order of millimeters. As, θ_{tx} , θ_{ty} , θ_{rx} , and θ_{ry} are all Gaussian random variables with non-zero

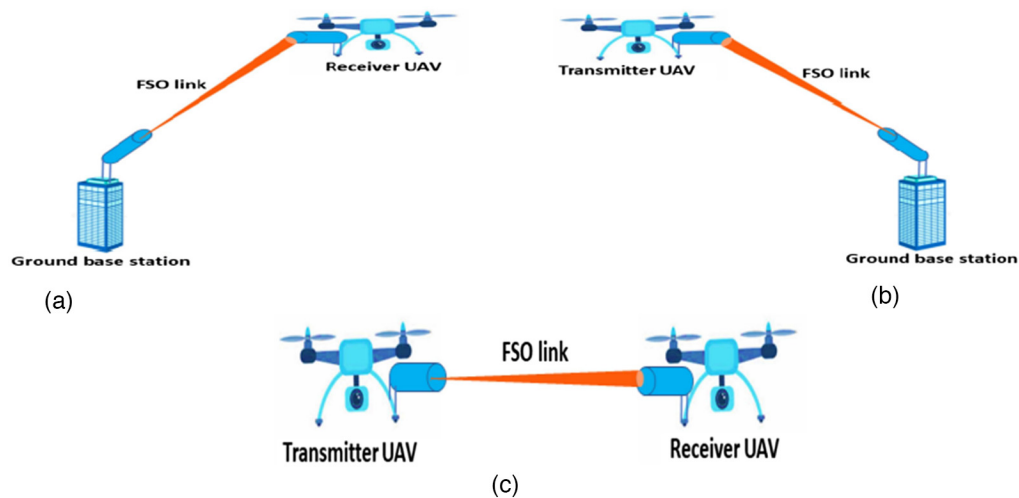


Fig. 6 Different link configurations (a) ground to UAV (G2U), (b) UAV to ground (U2G), and (c) UAV to UAV (U2U).

means and variances, AoA will have Beckmann distribution that can be nearly represented by the modified Rayleigh distribution as⁶⁰

$$f_{\theta_a}(\theta_a) \approx \frac{\theta_a}{\sigma_a^2} \exp\left(\frac{-\theta_a^2}{2\sigma_a^2}\right), \quad \theta_a \geq 0. \quad (27)$$

This pdf is valid for G2U and U2G links. In context of U2U links, the two random variables in x and y directions are modified as $\theta_{tx} + \theta_{rx}$ and $\theta_{ty} + \theta_{ry}$, respectively. Therefore, their means are $\mu_{tx} + \mu_{rx}$ and $\mu_{ty} + \mu_{ry}$ and variances are $\sigma_{tx}^2 + \sigma_{rx}^2$ and $\sigma_{ty}^2 + \sigma_{ry}^2$. Thus, pdf can be expressed as

$$f_{\theta_a}(\theta_a) \approx \frac{\theta_a}{2\sigma_a^2} \exp\left(\frac{-\theta_a^2}{4\sigma_a^2}\right), \quad \theta_a \geq 0. \quad (28)$$

Here, the displacement variance, σ_a^2 , takes a similar form as given by the last row of Table 4. It can thus be observed that the number of random variables required for a UAV based FSO system is way larger as compared to an FSO system.

The pdf of AoA fluctuations can, therefore, be interpreted as⁶⁴

$$f_{h_o}(h_o) = \exp\left(-\frac{\theta_{\text{FoV}}^2}{2\sigma_a^2}\right)\delta(h_o) + \left[1 - \exp\left(-\frac{\theta_{\text{FoV}}^2}{2\sigma_a^2}\right)\right]\delta(h_o - 1). \quad (29)$$

This is for G2U and U2G cases. Similarly for U2U scenario, the above pdf can be expressed as

$$f_{h_o}(h_o) = \exp\left(-\frac{\theta_{\text{FoV}}^2}{4\sigma_a^2}\right)\delta(h_o) + \left[1 - \exp\left(-\frac{\theta_{\text{FoV}}^2}{4\sigma_a^2}\right)\right]\delta(h_o - 1). \quad (30)$$

Here, $\delta(\cdot)$ is the Dirac Delta function.

4.5 Overall Channel Impairment in UAV-based FSO Systems

The statistical channel analysis of UAV-based FSO links for determining the various performance metrics can be carried out by evaluating the overall channel state. So far we have seen all the four channel effects that mainly affect the performance of any UAV-based FSO link. The attenuation of the received signal is caused due to the combined impact of these four impairments. These effects are considered independent of each other; therefore, the overall channel state can be computed through the multiplication of these individual channel impairments. It can occur to the mind that as the orientation deviations of the transmitter UAV form a component of both the pointing errors and AoA fluctuations, there must be some correlation between the two. But in reality, this relation is quite weak because $\theta_{\text{FoV}} \gg \sigma_a$, i.e., the receiver's field of view is very large as compared to the standard deviation caused by the orientation fluctuations. Typical values of θ_{FoV} are in the order of mrad; whereas, the transceiver's orientation deviations lie in the range of μrad . Thus, the overall channel state information, h , can be obtained as⁶⁴

$$h = h_a h_t h_p h_o. \quad (31)$$

The pdf of this channel can be determined as⁶⁴

$$f_h(h) = \int_0^\infty \frac{1}{h'} f_{h_o}\left(\frac{h}{h'}\right) f_{h'}(h') dh', \quad (32)$$

where $h' = h_a h_t h_p$. This expression can be obtained using Bayes' rule and concepts of transformation of random variables. For moderate to strong turbulence induced fading, the combined pdf can be expressed using Gamma-Gamma distribution as³⁷

$$\begin{aligned}
f_h(h) \approx & \exp\left(-\frac{\theta_{\text{FoV}}^2}{2\sigma_a^2}\right)\delta(h) \\
& + \left[1 - \exp\left(-\frac{\theta_{\text{FoV}}^2}{2\sigma_a^2}\right)\right] \frac{\alpha\beta\zeta^2}{A_0 h_a \Gamma(\alpha)\Gamma(\beta)} \\
& \times G_{1,3}^{3,0}\left(\frac{\alpha\beta}{A_0 h_a} h \middle| \zeta^2 - 1, \alpha - 1, \beta - 1\right), \quad (33)
\end{aligned}$$

where $G_{p,q}^{m,n}(\cdot)$ is the well-known Meijer-G function. The overall pdf can also be expressed in a more generalized way, valid for all turbulence regimes, using \mathcal{M} distribution, as⁶⁰

$$\begin{aligned}
f_h(h) \approx & \exp\left(-\frac{\theta_{\text{FoV}}^2}{2\sigma_a^2}\right)\delta(h) \\
& + \left[1 - \exp\left(-\frac{\theta_{\text{FoV}}^2}{2\sigma_a^2}\right)\right] \frac{\zeta^2 A_M}{2h} \sum_{m=1}^{\beta} a_m \left(\frac{\alpha\beta}{g\beta + \Omega'}\right)^{-\frac{(\alpha+m)}{2}} \\
& \times G_{1,3}^{3,0}\left(\frac{\alpha\beta h}{(g\beta + \Omega')(h_a A_0)} \middle| \zeta^2 + 1\right)_{\zeta^2, \alpha, m}. \quad (34)
\end{aligned}$$

Thus, the overall channel impairment directly depends upon the small and large scale turbulence eddies, on the receiver's field of view, on the ratio of equivalent beamwidth and variance, on atmospheric attenuation, among other factors.

We know that AoA fluctuations and pointing errors together form GML. This GML depends on several link parameters such as aperture radius, beamwidth, boresight displacement, variance of position deviations and orientation deviations, beam's angle of arrival, and receiving end's field-of-view. GML plays a vital role in determining the link quality and reliability, for example, on increasing the boresight displacement or variance of radial displacement, the system performance is degraded. There are various geometric loss models used in the literature, some considering pointing error with zero boresight, some considering pointing error with a non-zero value of boresight, whereas, others are taking into account AoA fluctuations in addition to pointing errors. As per the need of specific scenarios, four significant geometric loss models are short-listed that can be realized for real-life situations and can be effectively utilized for upcoming research. Below, the details of these models are presented. Their specified models with mathematical representations, also depicting the impact of variation of different parameters of interest on the concerned performance metrics of FSO systems, are demonstrated in Table 6.

- (i) In case of ground-to-high altitude platform (HAP) links⁶⁸ or earth-to-satellite links, it is shown that in addition to the GML caused to the misalignment between transmitter and receiver, there is one more pointing error jitter variance induced due to beam wander. This beam wander induced pointing error is more probable in uplink than in downlink. The random displacements caused in the beam in x and y directions due to these beam wander effects are denoted by x_b and y_b , as shown in Fig. 7(a). They have Gaussian distribution with mean, 0 and variance given as

$$\sigma_b^2 = 2.07 \int_{h_0}^H C_n^2(l) (Z-l)^2 w_l^{-1/3} dl. \quad (35)$$

Here, H is the altitude of HAP, h_0 is the transmitter height, Z is the distance of propagation given as: $(H - h_0) \sec(\psi)$, ψ is the HAP zenith angle, and w_l is the beamwidth at distance, l . $C_n^2(l)$ is the structure parameter defining the variation of turbulence strength with altitude, given as

$$C_n^2(l) = 0.00594(V_w/27)^2(10^{-5}l)^{10}e^{-l/1000} + (2.7 \times 10^{-16})e^{-l/1500} + (C_0)e^{-l/100}, \quad (36)$$

where V_w is the wind velocity in m/s and C_0 is the value of $C_n^2(0)$, measured at ground, in $\text{m}^{-2/3}$. In this paper, AoA fluctuations are also considered.

Table 6 Summary of significant geometric loss models.

Reference	Key feature	Turbulence model	Mathematical representation	Parameter values considered	Results and explanation
68	Beam wander induced pointing error	Log-normal and Gamma-Gamma	$r_d = \sqrt{(x_d + x_b)^2 + (y_d + y_b)^2}$ $f_{r_d}(r_d) = \frac{r_d}{\sigma_r^2} \exp\left(-\frac{r_d^2}{2\sigma_r^2}\right), \sigma_r^2 = \sigma_m^2 + \sigma_b^2$	<ol style="list-style-type: none"> $\sigma_m = \{0.4, 0.6, 0.8\}$, $\psi = \{10^\circ, 20^\circ, 30^\circ, 40^\circ, 50^\circ, 60^\circ\}$ 	<ol style="list-style-type: none"> Determine optimal value of w_z with which maximum SNR can be achieved and an increase in optimal value of w_z can be seen with increasing σ_m, in order to compensate for the pointing error, 2. Effect of increase in beam wander caused by increasing ψ is observed as: an increase in value of ψ will give the same value of OP only by increasing P_t by 2 dBm.
69	Rotated ellipse aperture for eavesdropper	Gamma-Gamma	$\sigma_{me}^2 = \left(\frac{3}{2}\sigma_d^4\mu^2 + \sigma_d^6\right)^{1/3}, \nu_e = \frac{\sqrt{\pi}\sqrt{a^2 \cos^2 \theta \cos \phi}}{\sqrt{2}w_z}$ $A_e = \text{erf}(\nu_e) ^2 \exp\left(\frac{4\sigma_d(\sqrt{\mu^2 + \sigma_d^2 - \sigma_e} - 2\sigma_d)}{w_{eave}^2}\right)$	<ol style="list-style-type: none"> Normalized location of Eve, $(\mu_x/a, \mu_y/a) = \{(1,1), (4,1), (6,3)\}$, Normalized orientation of Eve, $\rho_r/a = \{0.4, 0.7, 1\}$ 	<ol style="list-style-type: none"> SOP is strongly dependent on ρ_r. Maximum SOP is obtained when $\rho_r = 1$. As ρ_r/a tends to zero, SOP decreases and outage capacity with no Eve is achieved, 2. Secrecy outage is less likely at higher values of SNR, when $\gamma_b > \gamma_e$.
27	Proportionate pointing error parameters for eavesdropper	Malaga	$\sigma_{de} = \frac{w}{L_b} \sigma_d, \mu_{txe} = \frac{w}{L_b} \mu_{tx}, \mu_{tve} = \frac{w}{L_b} \mu_{ty}$	<ol style="list-style-type: none"> $\mu = \{0.1, 0.5, 0.9, 1.2\}$ m, $\sigma_d = \{0.3, 0.6, 0.9, 1.2\}$ m 	<ol style="list-style-type: none"> SOP performance deteriorates with increasing values of μ and σ_d as an increase in these parameters implies increase in pointing error, 2. Scenario 1 is most sensitive to changes in σ_d as the performance will get most affected in the first case only.
70	UAV flying horizontally	Log-normal and Gamma-Gamma	$f_{\theta_a}(\theta_a) = \frac{\theta_a \phi}{\sigma_a^2} \exp\left(-\frac{(\theta_a - \phi)^2}{2\sigma_a^2}\right),$ $\theta = \sqrt{(\theta_{tx} + \theta_{rx})^2 + (\theta_{ty} + \theta_{ty})^2}$	<ol style="list-style-type: none"> $\phi = \{0.5, 10, 20, 25\}$ mrad, Receiver UAV jitter angle variance, $\sigma_j^2 = \{0.1, 2.5, 7\}$ mrad 	<ol style="list-style-type: none"> Tilt angle of fuselage has greater effect on the communication quality of UAV than does the jitter induced by wind resistance, 2. OP and BER both increases with increase in the value of σ_j^2.

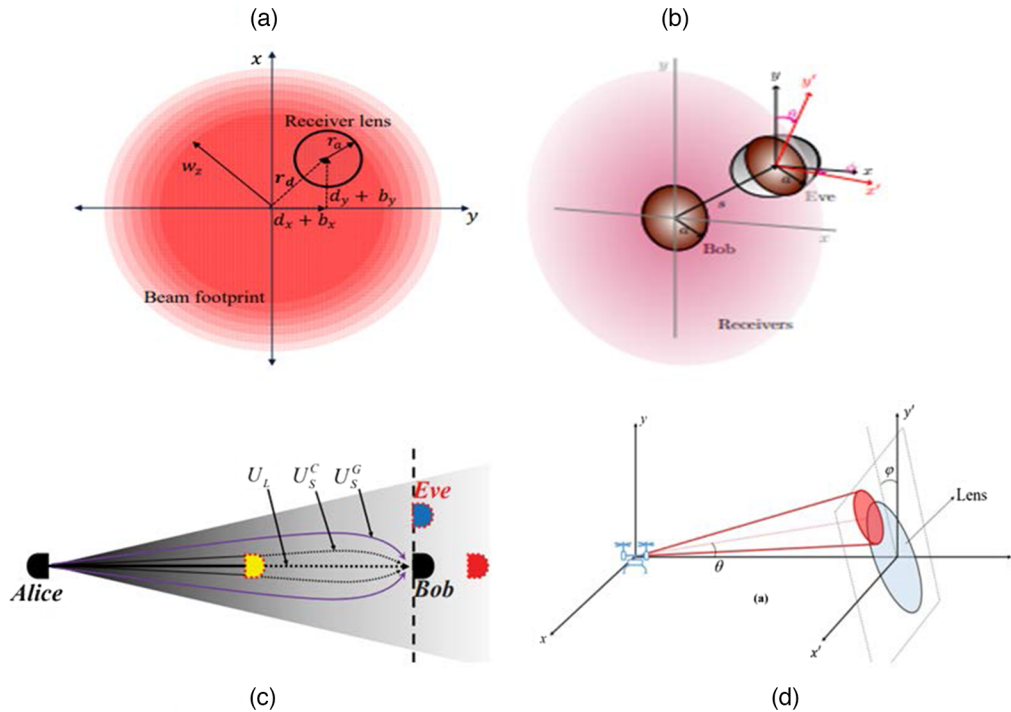


Fig. 7 Significant geometric loss models (a) beam wander induced pointing error, (b) rotated ellipse aperture of eavesdropper, (c) three different eavesdropping scenarios, and (d) tilt angle when UAV is flying horizontally.

- (ii) In Ref. 69, the case of wiretapping in FSO communication is considered. As the beamwidth is larger in FSO systems, they are prone to eavesdropping attacks. The eavesdropper (Eve) is assumed to be located near the receiver (Bob) such that the transmission distance is approximately the same for the receiver as well as for the eavesdropper. This is because of the assumption that the photo-detector's effective areas are situated in the same plane in which the incident beam is present in the x - y plane. Here, pointing error with zero boresight is considered for Bob, and Eve is assumed to be present in the inherent boresight displacement of Bob. For Bob, the incoming beam is thus perpendicular to the detector plane, but for Eve, the beam is not normal to the detector plane and for it, the non-zero boresight error model will have to be applied. The eavesdropper can appear in any of the orientations leading to a rotation in x -direction by an angle, θ and/or rotation in y -direction by an angle, ϕ , therefore, the fraction of captured power by Eve is not a function of the circular aperture but it is now determined by the rotated ellipse aperture whose first axis is given by: a and the second axis can be expressed as: $a \cos \theta \cos \phi$. This second axis is also known as rotation parameter, denoted by ρ_r . This model is shown in Fig. 7(b).
- (iii) Three different cases of eavesdropper's location are considered in Ref. 27, first when Eve is present between Alice and Bob, second when it is present in the same receiving plane as Bob, and third when it is situated behind Bob as depicted in Fig. 7(c). \mathcal{M} distribution model from Ref. 61 is considered to account for the fading effect due to scintillation. Non-zero boresight pointing error model is considered both for Bob and Eve, and the analysis is carried out for all three cases. The mean displacement in Eve's position in x and y directions and its jitter variance are assumed to be in proportion to the ratio of link length of Eve and Bob and to the corresponding parameters associated with Bob.
- (iv) When the receiver UAV is flying horizontally,⁷⁰ the AoA between the center of the beam and the receiver is not only affected by jitter induced by pointing errors but also by the tilt angle of the receiver plane as demonstrated in Fig. 7(d). Thus, the modified AoA becomes: $(\theta - \phi)$, where θ denotes the beam AoA and ϕ represents the tilt angle. In this brief, pointing error with non-zero boresight is taken into account in addition to the AoA fluctuations.

5 Performance Metrics of UAV-Based FSO Systems

For any communication technique, reliability is of utmost importance. The data sent should efficiently reach the destination with a minimum probability of error. FSO systems offer a high level of signal-to-noise ratio (SNR) for both terrestrial and space communication, which in turn can provide a high transmission rate. There are several factors, as discussed above, that limit the performance of these systems including scattering, absorption, transceiver misalignment, and turbulence induced fading. Out of these, the turbulence is the main reason for signal deterioration at the receiver resulting in poor link reliability. These phenomena cause fluctuations in the signal strength and phase that severely deteriorate the overall system performance. Channel state information is an essential requirement for determining the SNR at the receiver, which ultimately leads to the computation of the various performance metrics of the optical link. The signal at the destination can be expressed as

$$y = (RhP_t x_t)^{c/2} + n, \quad (37)$$

where R is the responsivity of the detector, h is the overall channel impulse response, x_t is transmitted symbol $\in \{0,1\}$, P_t is the average source transmit power, n represents the AWGN with zero mean and variance, σ_n^2 , which is independent of the signal and the value of the parameter, c , is 1 for heterodyne detection (HD) and its 2 for intensity modulation/direct detection (IM/DD).⁶⁰ Therefore, the instantaneous SNR for the case of IM/DD receiver can be given as $\gamma = \frac{2P_t^2 R^2 h^2}{\sigma_n^2}$ and thus, the average SNR in absence of fading is given by $\bar{\gamma} = \frac{P_t^2 R^2}{2\sigma_n^2}$. The reliability of optical wireless links can be measured in terms of some performance metrics, such as bit error rate (BER), secrecy rate, outage probability, secrecy outage probability (SOP), ergodic capacity, etc. These parameters are defined for an HD receiver as follows:

5.1 Bit Error Rate

BER of a given link in terms of instantaneous SNR can be calculated as

$$P_e = \int_0^\infty \mathcal{P}(e/\gamma) f_\gamma(\gamma) d\gamma. \quad (38)$$

Here, $f_\gamma(\gamma)$ can be computed using Eq. (34) by applying the concept of transformation of random variables. For ON/OFF keying, the error probability, $P(e/\gamma)$, can be expressed as

$$P(e/\gamma) = \frac{1}{2} \operatorname{erfc}\left(\sqrt{\frac{\gamma}{2}}\right), \quad (39)$$

where the complementary error function, $\operatorname{erfc}(\cdot)$ can be written in the form of Meijer-G function as follows:

$$P(e/\gamma) = \frac{1}{2\sqrt{\pi}} G_{1,2}^{2,0}\left(\frac{\gamma}{2} \middle| \frac{1}{0, 0.5}\right). \quad (40)$$

On putting the values from Eqs. (40) and (34) into Eq. (38) and using the identity from Ref. 71 for solving the integral, the expression for BER can be obtained in closed form as

$$P_e = \frac{1}{2} \exp\left(-\frac{\theta_{\text{FoV}}^2}{2\sigma_a^2}\right) + \left[1 - \exp\left(-\frac{\theta_{\text{FoV}}^2}{2\sigma_a^2}\right)\right] \times \frac{\zeta^2 A_M}{4\sqrt{\pi}} \sum_{m=1}^{\beta} a_m \left(\frac{\alpha\beta}{g\beta + \Omega'}\right)^{-\frac{(\alpha+m)}{2}} G_{3,4}^{3,2}\left(\frac{2A^2}{\bar{\gamma}} \middle| 1, 0.5, \zeta^2 + 1\right), \quad (41)$$

where $\bar{\gamma}$ is the average value of SNR and the parameter A is given as follows:

$$A = \frac{\zeta^2}{\zeta^2 + 1} (g + \Omega') \left[1 - \exp\left(-\frac{\theta_{\text{FoV}}^2}{2\sigma_a^2}\right)\right] \frac{\alpha\beta}{(g\beta + \Omega')}.$$

Reference 60 compares the symbol error rate for G2U, U2G, and U2U links, and it is concluded that error rate is worst in case of U2U links as AoA fluctuations are maximum for such links.

5.2 Normalized Ergodic Capacity

Atmospheric turbulence is a slow fading phenomenon. Channel's coherence time lies in the order of milliseconds and thus, fading caused due to turbulence can be assumed to be almost the same for the transmission of a huge bit number. Ergodic capacity gives the upper limit on obtainable capacity, determined by averaging the instantaneous capacity of the channel up to infinite time. The ergodic capacity of a UAV-employed FSO link can thus be defined as⁷²

$$C_{\text{erd}} = \mathbb{E}[\log_2(1 + b\gamma)] = \int_0^{\infty} \log_2(1 + b\gamma) f_{\gamma}(\gamma) d\gamma, \quad (42)$$

where b is a constant, $b = 1$ for HD receiver, and $b = \frac{e}{2\pi}$ for DD receiver. Logarithmic function can be written in the form of Meijer-G function as follows:

$$\log_2(1 + b\gamma) = \frac{1}{\ln(2)} G_{2,2}^{1,2} \left(b\gamma \middle| \begin{matrix} 1, 1 \\ 1, 0 \end{matrix} \right). \quad (43)$$

Now substituting the values from Eqs. (43) and (34) into Eq. (42) and using the identity from Ref. 71 for solving the integral, we get

$$C_{\text{erd}} = \left[1 - \exp\left(-\frac{\theta_{\text{FoV}}^2}{2\sigma_a^2}\right) \right] \frac{\zeta^2 A_M}{2 \ln(2)} \sum_{m=1}^{\beta} a_m \left(\frac{\alpha\beta}{g\beta + \Omega'} \right)^{-\frac{(\alpha+m)}{2}} \\ \times G_{3,5}^{5,1} \left(\frac{A}{b\bar{\gamma}} \middle| \begin{matrix} 0, 1, \zeta^2 + 1 \\ \zeta^2, \alpha, m, 0, 0 \end{matrix} \right). \quad (44)$$

References 36, 72, and 73 specifically focus on ergodic capacity analysis in FSO systems and highlight the different parameters that need to be optimized for obtaining a desired value of ergodic capacity.

5.3 Outage Probability

It is the probability with which the instantaneous SNR gets less than a pre-calculated threshold value, γ_{th} . Thus, the outage probability can be written as⁶⁶

$$P_{\text{out}}(\gamma_{\text{th}}) = \mathcal{P}(\gamma < \gamma_{\text{th}}) = F_{\gamma}(\gamma_{\text{th}}), \quad (45)$$

where $F_{\gamma}(\gamma_{\text{th}})$ represents the cumulative distribution function (CDF) of instantaneous SNR calculated at γ_{th} .

From the PDF of Eq. (34), CDF can be obtained by using the identity from Ref. 71. Thus, the CDF of γ at γ_{th} can be written as

$$P_{\text{out}}(\gamma_{\text{th}}) = \exp\left(-\frac{\theta_{\text{FoV}}^2}{2\sigma_a^2}\right) + \left[1 - \exp\left(-\frac{\theta_{\text{FoV}}^2}{2\sigma_a^2}\right) \right] \frac{\zeta^2 A_M}{2} \\ \times \sum_{m=1}^{\beta} a_m \left(\frac{\alpha\beta}{g\beta + \Omega'} \right)^{-\frac{(\alpha+m)}{2}} G_{2,4}^{3,1} \left(\frac{A\gamma_{\text{th}}}{\bar{\gamma}} \middle| \begin{matrix} 1, \zeta^2 + 1 \\ \zeta^2, \alpha, m, 0 \end{matrix} \right). \quad (46)$$

References 34, 35, 37, and 64 explicitly analyze outage probability in FSO networks and demonstrate various parameters upon which outage probability depends.

5.4 Secrecy Rate

It is a security metric that is concerned with maximizing the information transfer to legitimate receivers and minimizing it for malicious and illegitimate users.⁷⁴ The secrecy rate between the concerned receiver and the most detrimental eavesdropper is defined as⁶⁹

$$R_s = [R_r - R_e]^+, \quad (47)$$

where $[x]^+$ represents $\max\{x, 0\}$. R_r is the average rate of the concerned receiver and R_e is the average rate of the eavesdropper. Therefore, R_s can be written as

$$R_s = \log_2(1 + 4\bar{\gamma}_r h_r^2) - \log_2(1 + 4\bar{\gamma}_e h_e^2) = \log_2 \left(\frac{1 + 4\bar{\gamma}_r h_r^2}{1 + 4\bar{\gamma}_e h_e^2} \right), \quad (48)$$

where $\bar{\gamma}_r$ and $\bar{\gamma}_e$ represent the average SNRs of the receiver and the eavesdropper, respectively, and h_r and h_e denote the overall channel response for the receiver and the eavesdropper, respectively. References 27, 74, and 75 discuss secrecy capacity in detail and depict ways in which it can be maximized for FSO based systems.

5.5 Secrecy Outage Probability

Considering a passive attack scenario, where the transmitter and receiver have no information of the eavesdropper, transmitter cannot adapt the coding scheme of the eavesdropper and thus, it can only set a constant secrecy rate, R_{th} . When $R_s < R_{th}$, secrecy is compromised and an outage occurs. Otherwise, the link can achieve perfect secrecy. In case of outage, a security metric, SOP is defined for maintaining a secure link and this probability is given as²⁷

$$\begin{aligned} \text{SOP} &= \mathcal{P}(R_s < R_{th}) \\ &= \mathcal{P}\left(\log_2\left(\frac{1 + 4\bar{\gamma}_r h_r^2}{1 + 4\bar{\gamma}_e h_e^2}\right) < R_{th}\right) \\ &= \int_0^\infty F_{h_r}\left(\sqrt{\frac{2^{R_s}(1 + 4\bar{\gamma}_e h_e^2) - 1}{4\bar{\gamma}_r}}\right) f_{h_e}(h_e) dh_e. \end{aligned} \quad (49)$$

There are several papers that demonstrate the calculation and analysis of SOP for FSO links, including, Refs. 27, 76, 77, etc., determining the effect of various parameter variations on SOP.

A great deal of research work is done on the above mentioned performance metrics for an FSO link. Considering different turbulence conditions, different probability distributions for modeling turbulence, different system models, different modeling of geometric, and misalignment losses, these metrics are derived and verified with the simulation results. Depending on the presence or absence of boresight error, the impact of pointing errors is analyzed, and it is concluded that AoA fluctuations further have an adverse effect on link reliability. While designing the link, the various system parameters involved, can be optimized for achieving the desired values of the performance metrics. A summary of the work done in optimizing the various performance metrics for a UAV-employed FSO communication system is demonstrated in Table 7.

6 Latest Contributions in UAV-Based FSO Networks

Recently much work is done on the techniques that, when used in conjunction with UAV based FSO networks, can further provide performance enhancement of the link with minimum amount of overhead. They can either improve some metric of link performance measurement or they can contribute in increasing the coverage area in FSO systems. Three such techniques are explained in detail in this section.

6.1 Continuous Variable Quantum Key Distribution

Quantum key distribution (QKD) is a well-established technique for providing unconditional security against eavesdropping in FSO networks. Due to the misalignment of source and destination, caused because of several reasons and due to the growing beamwidth with distance, the security aspect of FSO networks cannot be overlooked. Also, the small size and weight of optical devices make this issue even more crucial as any Eve intercepts the channel and overhears the transmitted information. QKD, using the principles of quantum mechanics, offers a promising answer to exchange a secret key between the two legitimate nodes, Alice and Bob. It relies on transmission of non-orthogonal quantum states. Using a dedicated transmission protocol, first the information is prepared, then transmitted over the public channel, and measured for the purpose of key distribution. This is followed by classical post-processing involving sifting, error correction, and privacy amplification. QKD can be implemented majorly using two methods: continuous-variable (CV) and discrete-variable (DV). DVQKD employs single photon states for information coding purpose while CVQKD employs coherent states^{83–85} in which information on the key is coded in terms of amplitude or phase of weakly modulated light pulses. Although, DVQKD offers key distribution up to long distances but it has a major drawback of requiring single photon detectors, which are expensive as well as bulky. Thus, CVQKD is preferred as they enable high key rates using homodyne/HD.

Table 7 Summary of the work done in optimizing the various performance metrics of UAV-based FSO communication systems.

Reference	Turbulence model	Boresight error	Metric	Key parameters varied	Inferences
60	Malaga	Yes	Outage probability, ergodic capacity, and symbol error rate	Link distance, w_z , and σ_a	U2U link performance is worst in terms of all the discussed performance metrics
37	Gamma-Gamma	No	Link and end-to-end outage probability	σ_R^2 , P_t , and number of relays, N	When $\theta_{FoV} \geq 5\sigma_a$, analytical and simulation results match perfectly
62	Log-normal and Gamma-Gamma	Yes	BER	σ_m^2/a , and w_z/a	Based on asymptotic analysis, boresight error results in an SNR penalty on system performance and diversity order is determined by w_{eq} and σ_m
64	Log-normal and Gamma-Gamma	No	Outage probability and BER	θ_{FoV} , P_t , and σ_R^2	Optimal design of FSO communication system employing UAV can be done using a tractable channel model and validity of model is proved especially for larger FoVs
35	Log-normal	No	Outage probability	UAV's instability, σ_θ , θ_{div} , and elevation angle of destination, ψ_d	The optimal values of σ_θ came out to be 5 and 10 mrad and on increasing the optimal value of σ_θ , the ratio, $\frac{\theta_{div}}{\theta_{opt}}$ changes from 28.6 to 76
34	Gamma-Gamma	Yes	BER and outage probability	Relay gain, G , σ_{dx} , σ_{dy} , a , w_d , w_s , and σ_R^2	The optimal value of w_s can be expressed as: $J_1 < w_s < 3J_1$, where J_1 is the resultant variance of position deviations of transmitter and receiver in x and y directions
59	Malaga	No	Outage probability	Coupling parameter, ρ , and blocking probability, P_b	The effect of blocking LoS on outage probability reduces as the turbulence strength increases
78	Negative exponential	No	BER and outage probability	Number of transmitter receiver apertures, M , and N	BER decreases with increasing w_{eq} and it continues to decrease till a specific value of w_{eq} . At $\gamma_{avg} = 0$ dB, $w_{eq} = 5.5$ m, and this specific value changes for different γ_{avg}
72	Log-normal, Malaga, and Rician log-normal	Yes	Ergodic capacity	μ , jitter variance, σ_j , ζ , and Rician turbulence parameter, k	As k increases, ergodic capacity improves and becomes equivalent to the log-normal case as $k \rightarrow \infty$

Table 7 (Continued).

Reference	Turbulence model	Boresight error	Metric	Key parameters varied	Inferences
79	Log-normal and Gamma-Gamma	No	Ergodic capacity, outage capacity, and BER	μ and σ_j	If $\mu > w_{eq}/\sqrt{2}$, non-zero jitter increases the received average power. The best value of σ_j^2 is obtained as: $\frac{2\mu^2 - w_{eq}^2}{4}$
77	Exponential Weibull	No	SOP and probability of positive secrecy capacity	Shape parameters, α and β , scale parameter, η , Nakagami fading severity parameter, m , a , and γ_e	Values of SOP increase monotonically because of higher impact of Eve caused due to increase in γ_e
36	Gamma-Gamma	No	Ergodic sum rate	UAV height above ground, z_d , α_v , MU density, λ , and w_0	The quality of FSO channel is not much affected by atmospheric turbulence for practical UAV to ground distances of <1 km and for high λ , available bandwidth for each MU decreases, thus, SNR increases, thereby improving the ergodic rate of the channel
80	Gamma-Gamma	No	Outage probability and BER	Average SNR per hop	At 40 dB, turbulence is weak and BER of proposed system is 1.1×10^{-6} , BER of RF-FSO system is 8.4×10^{-4} , and that of RF-RF/FSO system is 3.4×10^{-5}
73	Log-normal, Gamma-Gamma, and exponential Weibull	Yes	Asymptotic ergodic capacity	w_z/a , σ_j/a , d_{SD} , C_n^2 , and normalized spacing between RX apertures, d/a	FSO with multiple receivers can enhance capacity only if d is not too large. This is because it reduces the impact of non-zero inherent boresight
81	Gamma-Gamma	No	Outage probability, average BER, and average capacity	γ_{th}^{mix} , $\gamma_{th,UB}^{FSO}$, and $\gamma_{th,UB}^{FSO}$	For a target BER of 10^{-3} , SNR penalty of 6 dB is achieved in the case of dual FSO threshold as compared to single FSO threshold case when $\gamma_{th}^{FSO} = 5$ dB, $\gamma_{th,UB}^{FSO} = 2$ dB, and $\gamma_{th,UB}^{FSO} = 5$ dB
75	Malaga	No	Strictly positive secrecy capacity (SPSC), average secrecy capacity, and SOP	ζ and ρ	SPSC can be improved when ρ is increased as the turbulence intensity is reduced

Table 7 (Continued).

Reference	Turbulence model	Boresight error	Metric	Key parameters varied	Inferences
76	Malaga	No	Probability of non-zero secrecy capacity and SOP	α, β, ρ , Nakagami severity parameter, m , and γ_{avg}	Asymptotic slope of SOP curve is $\min\{\frac{\alpha}{2}, \frac{\beta}{2}\}$. Slope evidently depends on m and is independent of correlation condition
82	Log-normal Rician	No	Outage probability, ergodic capacity, and BER	Number of random variables, L , w_z/a , number of transmitters, M_t , and number of receivers, N_r	Optimum beamwidth derived, $w_{z,opt}/a$ is 6.7 when $L = 30$. Ergodic capacity for $M = 1$ and $N = 2$ is 5.54 b/s/Hz and for $M = 2$ and $N = 2$, it is 7.68 b/s/Hz
9	Log-normal	Yes	BER	Angular deviation, σ_j , and boresight, μ	BER only increases slightly when UAV height goes on increasing from 1 km and UAV kept at a certain height can avoid strong turbulence but the BER is still greater than 10^{-6}
63	Log-normal and Gamma-Gamma	Yes	Outage probability	w_z/a	Link margins of 3 and 2 dB are obtained at outage probability, P_{out} of 10^{-3} and 10^{-4} . $P_{out}(R_0, w_{z,opt})$ is computed at $R_0 = 0.5$ bits/channel use. Link margin of 5 dB is realized by optimizing w_z , when the system is designed to satisfy a P_{out} of 10^{-6}
66	Gamma-Gamma	Yes	Average outage probability and average BER	$w_z/a, (\mu_x/a, \mu_y/a), (\sigma_x/a, \sigma_y/a), d_{SD}$, and δ	Accuracy metric for P_{out} , M_{OP} is calculated. Higher value of M_{OP} is obtained when small jitter is present, of the order of 10^{-3} , otherwise achievable accuracy of 10^{-2} is obtained. Achievable accuracy becomes better as the parameter, δ increases

CVQKD based systems have been explored for various channels, such as noisy channels,⁸⁶ uniform fast fading channels,⁸⁷ etc. QKD protocol is also studied for FSO employing a dual-threshold (DT) DD receiver.⁸⁸ In Ref. 74, secrecy performance of FSO systems is evaluated for a DT receiver based on the quantum BER (QBER) and ergodic secrecy key rate (ESKR). Here, QBER is evaluated as

$$\text{QBER} = \frac{P_{\text{error}}}{P_{\text{sift}}}, \quad (50)$$

where P_{sift} is the sifting probability that the legitimate receiver can determine the bits from threshold detection. Also, the ESKR is given as the maximum rate for which the eavesdropper is not able to decrypt the transmitted data, and it is calculated as

$$\text{ESKR} = I(A; B) - I(A; E), \quad (51)$$

where $I(A; B)$ is the mutual information of Alice and Bob, and $I(A; E)$ is the mutual information of Alice and Eve, also known as Holevo quantity, representing the upper bound on the information that Eve possess on the shared key. In case ESKR is <0 , it implies that reliable connection is not feasible and no secret key can be shared. Here, the two design parameters chosen are intensity of modulation depth, δ_I (chosen at Alice's side) and DT scale coefficient, ζ_D . The values of these parameters and the conclusions drawn are presented in Table 8. In Ref. 89, the performance evaluation is done for UAV based FSO CVQKD systems using dual polarization quadrature phase shift keying with coherent detection. Here, Gaussian modulation of coherent states is employed as it is more effective against collective attacks. All types of channel impairments are considered for the analysis of QBER, raw key rate (RKR), and secrecy key rate (SKR). QBER is computed using Eq. (36) by taking the error probability for QPSK modulation scheme as

$$P(e/\gamma) = \frac{1}{2} \operatorname{erfc}(\sqrt{\gamma}h), \quad (52)$$

Table 8 Summary of results obtained with QKD protocols.

Reference	Parameter values considered	Results
74	For weak turbulence (W), $\delta_I \leq 0.25$, for moderate turbulence (M), $\delta_I \leq 0.31$, and for strong turbulence (S), $\delta_I \leq 0.45$	(1) For $P_{\text{sift}} \geq 10^{-2}$ and $\text{QBER} \leq 10^{-3}$, $0.71 \leq \zeta_D \leq 2.95(W)$, $0.16 \leq \zeta_D \leq 3.97(M)$, and $0 \leq \zeta_D \leq 6.27(S)$, smallest value of ζ_D is chosen such that SKR is positive for Eve's closest location to Bob. Thus, $P_{\text{sift}} = 0.252, 0.378$, and 0.361 (2) SKR = 8.374×10^{-4} , 5.6706×10^{-4} , and 1.3461×10^{-4} bits/channel for $d = 4.55, 3.45$, and 4.13 m. SKR increases if Eve is further moved away from Bob, i.e., for $d = 7$ m, SKR of $0.1785, 0.2839$, and 0.232 bits/channel is achieved for weak, moderate, and strong turbulence conditions.
89	(1) $\theta_{\text{div}} = \{1.5, 2.5\}$ mrad (2) $\theta_{\text{FoV}} = \{15, 20\}$ mrad (3) Variance of position deviations, $\sigma_p = \{5, 10\}$ cm (4) Variance of orientation deviations, $\sigma_o = \{3, 5\}$ mrad (5) $\langle T \rangle = \{0.6, 0.9\}$	(1) QBER $< 10^{-3}$ for $\theta_{\text{FoV}} = 20$ mrad, $P_t > 9$ dBm for $\theta_{\text{div}} = 2.5$ mrad and $P_t > 3$ dBm for $\theta_{\text{div}} = 1.5$ mrad, thus, for $P_t = 4$ dBm and $\theta_{\text{div}} = 1.5$ mrad, μ up to 7 cm is permissible (2) RKR = 7.2 and 11 b/s/Hz and SKR = 6.4 and 10 b/s/Hz for the two values of $\langle T \rangle$ (3) OP reaches threshold of 10^{-2} at $P_t > 3$ dBm for $\gamma_{\text{th}} = 5$ dB. At $P_t = 4$ dBm, $\gamma_{\text{th}} \leq 6.5$ dB, in order to keep the desired OP below threshold
90	(1) $\beta_R = \{0.9, 0.8, 0.5, 0.4\}$ (2) in case of decoy state BB-84, detection efficiency, $\eta_D = \{0.85, 0.25\}$	The proposed QKD protocol outperforms GM-CVQKD, DM (8 PSK) CVQKD, and decoy state BB-84 protocols

where $\bar{\gamma}$ is the average SNR for CVQKD employing HD. RKR and SKR are determined as

$$\begin{aligned} \text{RKR} &= (1 - \text{QBER})(\langle T \rangle \beta_R I_{AB}), \\ \text{SKR} &= (1 - \text{QBER})(\langle T \rangle \beta_R I_{AB} - I_{BE}). \end{aligned} \quad (53)$$

Here, β_R denotes the reconciliation efficiency and for the proposed system, reverse reconciliation (RR) is employed as the bits are corrected by Alice as per Bob's information. Also, $\langle T \rangle$ represents the transmittance of the channel. The optimal values of several parameters for maintaining a particular QBER and outage probability are demonstrated in Table 8. As per the work done in Ref. 90, a hybrid QKD protocol giving superior performance over both DVQKD and CVQKD techniques is presented. The problem with Gaussian modulation (GM) based CVQKD is low reconciliation efficiency, while with discrete modulation (DM) based CVQKD (uses a finite size of constellation), the issue of security proof requirement occurs. DVQKD already provides less transmission reach and low SKR values. So, in order to take advantage of high SKR values and large achievable transmission distance along with the acceptable absence of strict proof of security, a hybrid protocol is presented in which Alice simultaneously utilizes DM-CVQKD and phase-time encoding for DVQKD. At the receiver end, Bob uses a 1:2 optical switch to select between CVQKD or DVQKD. This selection is done on the basis of a selection probability, which is a function of the dead time of the single photon detector. A comparison among different QKD protocols is shown in terms of SKR and the proposed protocol outperformed in each case. CVQKD RKR is assumed to be 10 Gb/s and remaining parameter values are given in Table 8.

6.2 Intelligent Reflecting Surfaces

The motivation behind using intelligent reflecting surfaces (IRS) is the provision of LoS between source and destination. Sometimes when the transceivers are not in the LoS of each other, then an IRS can be used to reflect the light coming from the laser and direct it to the photodetector surface. A distribution of phase shift is taken as per which the light is reflected from the IRS according to the normal laws of reflection. Because of the blockage, an IRS-employed system is considered in which two- and three-dimensional models for the proposed system are demonstrated.²⁶ Also it is shown that a mirror can also be used to generate a reflected electric field equivalent to that of an IRS-employed system. Reference 24 extensively provides a review on re-configurable intelligent surfaces (RIS) carried UAV communication, which discusses the challenges with both RIS and UAV technologies and also highlights their future trends. Apart from increasing the coverage, RIS can be used to enhance the channel level state and resolve the problem of dead zones in RF communication. RIS used with UAVs can prove to be a boon for 6G communication. Due to analog and passive beamforming offered by RIS, it can be utilized in mmWave bands to maximize the minimum viable data rate of users. Other techniques, such as THz range communication, NOMA, machine learning, etc. can further be combined with RIS and UAV based systems in order to achieve better QoS, better performance, and improved security. In Ref. 25, a dual-hop all optical FSO system model is considered comprising of a transmitter and receiver communicating with the aid of a relay UAV assisted by an RORIS. The first hop is TX-RORIS-UAV link and the second hop is UAV-RX link. It is seen that the effect of RORIS can be observed on the GML and on atmospheric loss. In Ref. 91, for encountering the drawbacks of hybrid RF-FSO systems, i.e., when FSO link is blocked due to cloudy weather and inherent nature of RF links to offer comparatively low bandwidth, a new model involving HAP-assisted satellite aerial ground integrated network and RIS based UAV relay, is presented. Three strategies have been used for carrying out the communication between satellite, HAP, and ground station. First is the primary link defined as FSO-based satellite-HAP-ground link. The second one is the FSO-based satellite-HAP-UAV-ground link, used when the cloud liquid water content is high on the primary link, and third is the RF-based satellite-HAP-ground link, used when first two strategies cannot be implemented. In this brief, three types of aircraft systems are employed as per their distance from the earth's surface. Satellite is taken at a height of 600 km, HAP is taken at a height of 20 km, and UAV is positioned at a distance of 1 to 2 km. Ground station is considered at 50 m above the ground.

6.3 Modulating Retro-Reflectors

Modulating retro-reflector (MRR) provides significant advantages, such as decreasing the size, weight, and power requirements of the FSO link.⁹² A typical MRR consists of a light modulator and a retro-reflector. Generally in an FSO system, strict pointing, acquisition, and tracking (PAT) requirements are to be fulfilled at both sides of the link especially when simple UAV is used like a relay. At the relay, when MRR is used, PAT system is to be kept only at one side of the FSO link, thereby reducing the overhead. In the above-mentioned paper, a dual-hop mixed RF-FSO UAV based communication model is considered employing RIS and MRR. MRR is used at the relay and RIS works as a user or RF source containing an RF signal generator as well. Uplink and downlink both scenarios are considered here. RIS, when used in the RF link, containing many passive reflectors, enhances the signal quality and thus, improves the system performance. In Ref. 93, an FSO link of ground and a hovering UAV equipped with MRR is presented. The communication is to and fro. The overall channel irradiance for the complete communication link is computed considering the following impairments: atmospheric attenuation for both G2U and U2G links, turbulence induced fading for both G2U and U2G links, pointing error at the aperture of MRR, geometric loss at ground station, and the reflected power ratio by MRR.

7 Conclusion

Based on the above discussion, it can be inferred that UAV-based FSO communication is quite useful in providing high speed data transfer with massive connectivity. The minimization of optical devices and their low cost deployment has further supported their implementation in various fields of interest and diverse applications. Also, FSO systems are at high security risks owing to the fact that for a given divergence angle, the optical beam expands as it travels and this property makes them vulnerable to eavesdropping attacks. There are various impairments that degrade the free space channel and thus affect the signal quality and ultimately cause irradiance fluctuations in the received beam intensity.

In today's world, UAV is a trending technology that has tremendous applications in almost every sector and its market is growing at a rapid rate worldwide. It is most popularly employed as a relay of information due to its flying capability and LoS providing feature, whereas, in secrecy applications, it is often used as a jammer. In order to design and maintain a good quality UAV-based FSO link, it is important to consider some performance metrics, which as a function of SNR or channel gain, give useful insights on the variation of several system parameters, such as receiver's field of view, beam waist. There are techniques, such as CVQKD, MRR, and IRS, which can be combined with UAV and FSO networks to further enhance the system performance in order to carry out the communication in a more efficient manner. It can be seen that different models can be utilized to replicate the real-life scenarios as closely as possible and compute the respective parameters. Research work can be carried out on the pointing, acquisition, and tracking (PAT) system for UAVs so that the error caused due to misalignment can be reduced to a minimum and more technologies can be explored for UAV based FSO systems, such as NOMA, CR, etc. for further improving the system throughput and network reliability.

Data Availability Statement

Since it is a review paper, there is no supporting data to be provided for this paper.

Acknowledgments

There is no conflict of interest between the authors, and there is no financial or non-financial assistance taken from any third party for the reported work.

References

1. A. K. Majumdar, *Advanced Free Space Optics (FSO): A Systems Approach*, Vol. 186, Springer (2014).
2. H. Kaushal, V. Jain, and S. Kar, *Free Space Optical Communication*, Springer (2017).
3. S. A. Al-Gailani et al., "A survey of free space optics (FSO) communication systems, links, and networks," *IEEE Access* 9, 7353–7373 (2020).

4. M. A. Khalighi and M. Uysal, "Survey on free space optical communication: a communication theory perspective," *IEEE Commun. Surv. Tut.* **16**(4), 2231–2258 (2014).
5. A. Jahid, M. H. Alsharif, and T. J. Hall, "A contemporary survey on free space optical communication: potentials, technical challenges, recent advances and research direction," *J. Netw. Comput. Appl.* **200**, 103311 (2022).
6. H. Kaushal and G. Kaddoum, "Optical communication in space: challenges and mitigation techniques," *IEEE Commun. Surv. Tut.* **19**(1), 57–96 (2016).
7. S. Kumar and N. Sharma, "Emerging military applications of free space optical communication technology: a detailed review," *J. Phys. Conf. Ser.* **2161**(1), 012011 (2022).
8. M. Alzenad et al., "FSO-based vertical backhaul/fronthaul framework for 5G+ wireless networks," *IEEE Commun. Mag.* **56**(1), 218–224 (2018).
9. M. Li et al., "Investigation on the UAV-to-satellite optical communication systems," *IEEE J. Sel. Areas Commun.* **36**(9), 2128–2138 (2018).
10. S. Zhang and J. Liu, "Analysis and optimization of multiple unmanned aerial vehicle-assisted communications in post-disaster areas," *IEEE Trans. Veh. Technol.* **67**(12), 12049–12060 (2018).
11. A. Amphawan et al., "Post-flood UAV-based free space optics recovery communications with spatial mode diversity," *Electronics* **11**(14), 2257 (2022).
12. W. Fawaz, C. Abou-Rjeily, and C. Assi, "UAV-aided cooperation for FSO communication systems," *IEEE Commun. Mag.* **56**(1), 70–75 (2018).
13. C. Chen et al., "High-speed optical links for UAV applications," *Proc. SPIE* **10096**, 316–324 (2017).
14. X. Zhang, Q. Zhu, and H. V. Poor, "Average coverage probability for base-station-to-UAV communications over 6G multiple access wireless networks," in *IEEE Int. Symp. on Inf. Theory (ISIT)*, IEEE, pp. 748–753 (2022).
15. J.-H. Lee et al., "A UAV-mounted free space optical communication: trajectory optimization for flight time," *IEEE Trans. Wirel. Commun.* **19**(3), 1610–1621 (2019).
16. A. Zheng, Y. Huang, and S. Gao, "Modeling and spatial diversity-based receiving improvement of in-flight UAV FSO communication links," *Appl. Sci.* **11**(14), 6365 (2021).
17. K. Kazaura et al., "Mitigation of atmospheric effects on terrestrial FSO communication systems by using high-speed beam tracking antenna," *Proc. SPIE* **6105**, 167–176 (2006).
18. K. Kazaura et al., "Performance evaluation of next generation free-space optical communication system," *IEICE Trans. Electron.* **E90-C**(2), 381–388 (2007).
19. R. Abdelfatah, N. Alshaer, and T. Ismail, "A review on pointing, acquisition, and tracking approaches in UAV-based FSO communication systems," *Opt. Quantum Electron.* **54**(9), 571 (2022).
20. A. Tosun, H. Nouri, and M. Uysal, "Experimental investigation of pointing errors on drone-based FSO systems," in *28th Signal Process. and Commun. Appl. Conf. (SIU)*, IEEE, pp. 1–4 (2020).
21. M. N. Sadiku, S. M. Musa, and S. R. Nelatury, "Free space optical communications: an overview," *Eur. Sci. J.* **12**(9), 55–68 (2016).
22. H. Kaushal et al., "Experimental investigation of optimum beam size for FSO uplink," *Opt. Commun.* **400**, 106–114 (2017).
23. D. Wu, X. Sun, and N. Ansari, "An FSO-based drone assisted mobile access network for emergency communications," *IEEE Trans. Netw. Sci. Eng.* **7**(3), 1597–1606 (2019).
24. N. Rahmatov and H. Baek, "RIS-carried UAV communication: current research, challenges, and future trends," *ICT Express* (2023).
25. P. Saxena and Y. H. Chung, "On the performance of all-optical RORIS dual hop UAV based FSO systems," *ICT Express* **9**(3), 466–472 (2022).
26. M. Najafi, B. Schmauss, and R. Schober, "Intelligent reflecting surfaces for free space optical communication systems," *IEEE Trans. Commun.* **69**(9), 6134–6151 (2021).
27. H. Wu et al., "Secrecy performance analysis in the FSO communication system considering different eavesdropping scenarios," *Opt. Express* **30**(23), 41028–41047 (2022).
28. M. N. Boukoberine, Z. Zhou, and M. Benbouzid, "A critical review on unmanned aerial vehicles power supply and energy management: solutions, strategies, and prospects," *Appl. Energy* **255**, 113823 (2019).
29. X. He et al., "Resource allocation for secrecy rate optimization in UAV-assisted cognitive radio network," in *IEEE Wirel. Commun. and Netw. Conf. (WCNC)*, IEEE, pp. 1–6 (2021).
30. M. T. Dabiri et al., "Analytical channel models for millimeter wave uav networks under hovering fluctuations," *IEEE Trans. Wirel. Commun.* **19**(4), 2868–2883 (2020).
31. M. Najafi et al., "Non-orthogonal multiple access for FSO backhauling," in *IEEE Wirel. Commun. and Netw. Conf. (WCNC)*, IEEE, pp. 1–6 (2018).
32. Z. Yin et al., "Max-min secrecy rate for NOMA-based UAV-assisted communications with protected zone," in *IEEE Glob. Commun. Conf. (GLOBECOM)*, IEEE, pp. 1–6 (2019).
33. J.-H. Lee et al., "Throughput maximization of mixed FSO/RF UAV-aided mobile relaying with a buffer," *IEEE Trans. Wirel. Commun.* **20**(1), 683–694 (2020).

34. M. T. Dabiri et al., "UAV-assisted free space optical communication system with amplify-and-forward relaying," *IEEE Trans. Veh. Technol.* **70**(9), 8926–8936 (2021).
35. M. T. Dabiri and S. M. S. Sadough, "Optimal placement of UAV-assisted free-space optical communication systems with DF relaying," *IEEE Commun. Lett.* **24**(1), 155–158 (2019).
36. H. Ajam et al., "Ergodic sum rate analysis of UAV-based relay networks with mixed RF-FSO channels," *IEEE Open J. Commun. Soc.* **1**, 164–178 (2020).
37. J.-Y. Wang et al., "Hovering UAV-based FSO communications: channel modelling, performance analysis, and parameter optimization," *IEEE J. Sel. Areas Commun.* **39**(10), 2946–2959 (2021).
38. P. Lohan et al., "Secrecy-aware UAV position-aided jamming for practical eavesdropper localization models," *Veh. Commun.* **33**, 100430 (2022).
39. H. K. Narsani et al., "Leveraging UAV-assisted communications to improve secrecy for URLLC in 6G systems," *Digital Commun. Netw.* (2022).
40. X. Zhou et al., "UAV-enabled secure communications: joint trajectory and transmit power optimization," *IEEE Trans. Veh. Technol.* **68**(4), 4069–4073 (2019).
41. Y. Zhu, G. Zheng, and M. Fitch, "Secrecy rate analysis of UAV-enabled mmwave networks using Matérn hardcore point processes," *IEEE J. Sel. Areas Commun.* **36**(7), 1397–1409 (2018).
42. T. Bao, H.-C. Yang, and M. O. Hasna, "Secrecy performance analysis of UAV-assisted relaying communication systems," *IEEE Trans. Veh. Technol.* **69**(1), 1122–1126 (2019).
43. M. Li et al., "Secrecy energy efficiency maximization in UAV-enabled wireless sensor networks without eavesdropper's CSI," *IEEE Internet Things J.* **9**(5), 3346–3358 (2021).
44. V. P. Tuan, N. Q. Sang, and H. Y. Kong, "Secrecy capacity maximization for untrusted UAV-assisted cooperative communications with wireless information and power transfer," *Wirel. Netw.* **26**, 2999–3010 (2020).
45. Z. Wang et al., "Robust secure UAV relay-assisted cognitive communications with resource allocation and cooperative jamming," *J. Commun. Netw.* **24**(2), 139–153 (2022).
46. S. K. Singh et al., "On UAV selection and position-based throughput maximization in multi-UAV relaying networks," *IEEE Access* **8**, 144039–144050 (2020).
47. Y. Li et al., "Cooperative jamming for secure UAV communications with partial eavesdropper information," *IEEE Access* **7**, 94593–94603 (2019).
48. Q. Wang et al., "Joint power and trajectory design for physical-layer secrecy in the UAV-aided mobile relaying system," *IEEE Access* **6**, 62849–62855 (2018).
49. S. Ahmed and B. A. Bash, "Average worst-case secrecy rate maximization via UAV and base station resource allocation," in *57th Annu. Allerton Conf. Commun., Control, and Comput. (Allerton)*, IEEE, pp. 1176–1181 (2019).
50. H. Bastami et al., "On the physical layer security of the cooperative rate-splitting-aided downlink in UAV networks," *IEEE Trans. Inf. Forensics Security* **16**, 5018–5033 (2021).
51. M. Cheng et al., "Effects of asymmetry atmospheric eddies on spreading and wander of Bessel–Gaussian beams in anisotropic turbulence," *IEEE Photonics J.* **10**(3), 6100510 (2018).
52. J. K. Sahota and D. Dhawan, "Reducing the effect of scintillation in FSO system using coherent based homodyne detection," *Optik* **171**, 20–26 (2018).
53. J. K. Sahota and D. Dhawan, "Analyzing the effect of scintillation on free space optics," *Internal J. Recent Innov. Trends Comput. Commun.* **5**(6), 493–496 (2017).
54. L. C. Andrews et al., "Theory of optical scintillation," *JOSA A* **16**(6), 1417–1429 (1999).
55. E. Jarangal and D. Dhawan, "Comparison of channel models based on atmospheric turbulences of FSO system: a review," *Int. J. Res. Electron. Comput. Eng.* **6**(1), 282–286 (2018).
56. K. Anbarasi, C. Hemanth, and R. Sangeetha, "A review on channel models in free space optical communication systems," *Opt. Laser Technol.* **97**, 161–171 (2017).
57. A. Jurado-Navas et al., "A unifying statistical model for atmospheric optical scintillation," *Numer. Simul. Phys. Eng. Process.* **181**(8), 181–205 (2011).
58. N. Alshaer, T. Ismail, and M. E. Nasr, "Generic evaluation of FSO system over Málaga turbulence channel with MPPM and non-zero-boresight pointing errors," *IET Commun.* **14**(18), 3294–3302 (2020).
59. J. M. Garrido-Balsells et al., "Performance analysis of FSO communications under LOS blockage," *Opt. Express* **25**(21), 25278–25294 (2017).
60. D. Singh and R. Swaminathan, "Comprehensive performance analysis of hovering UAV-based FSO communication system," *IEEE Photonics J.* **14**(5), 7352013 (2022).
61. J. M. Garrido-Balsells et al., "Novel formulation of the model through the generalized-k distribution for atmospheric optical channels," *Opt. Express* **23**(5), 6345–6358 (2015).
62. F. Yang, J. Cheng, and T. A. Tsiftsis, "Free-space optical communication with nonzero boresight pointing errors," *IEEE Trans. Commun.* **63**(2), 713–725 (2014).
63. A. A. Farid and S. Hranilovic, "Outage capacity optimization for free-space optical links with pointing errors," *J. Lightwave Technol.* **25**(7), 1702–1710 (2007).

64. M. T. Dabiri, S. M. S. Sadough, and I. S. Ansari, "Tractable optical channel modeling between UAVS," *IEEE Trans. Veh. Technol.* **68**(12), 11543–11550 (2019).
65. M. T. Dabiri et al., "Channel modeling for UAV-based optical wireless links with nonzero boresight pointing errors," *IEEE Trans. Veh. Technol.* **69**(12), 14238–14246 (2020).
66. R. Boluda-Ruiz et al., "Novel approximation of misalignment fading modeled by Beckmann distribution on free-space optical links," *Opt. Express* **24**(20), 22635–22649 (2016).
67. H. G. Sandalidis, T. A. Tsiftsis, and G. K. Karagiannidis, "Optical wireless communications with heterodyne detection over turbulence channels with pointing errors," *J. Lightwave Technol.* **27**(20), 4440–4445 (2009).
68. H. Safi et al., "Analytical channel model and link design optimization for ground-to-hap free-space optical communications," *J. Lightwave Technol.* **38**(18), 5036–5047 (2020).
69. R. Boluda-Ruiz et al., "Secure communication for FSO links in the presence of eavesdropper with generic location and orientation," *Opt. Express* **27**(23), 34211–34229 (2019).
70. M. R. Hayal et al., "Modeling and investigation on the performance enhancement of hovering UAV-based FSO relay optical wireless communication systems under pointing errors and atmospheric turbulence effects," *Opt. Quantum Electron.* **55**(7), 625 (2023).
71. Wolfram-Research, *Mathematica Edition: Version 8.0*, Wolfram-Research, Inc., Champaign, Illinois (2010).
72. I. S. Ansari, M.-S. Alouini, and J. Cheng, "Ergodic capacity analysis of free-space optical links with nonzero boresight pointing errors," *IEEE Trans. Wirel. Commun.* **14**(8), 4248–4264 (2015).
73. R. Boluda-Ruiz et al., "Impact of nonzero boresight pointing error on ergodic capacity of MIMO FSO communication systems," *Opt. Express* **24**(4), 3513–3534 (2016).
74. P. V. Trinh et al., "Secrecy analysis of FSO systems considering misalignments and eavesdropper's location," *IEEE Trans. Commun.* **68**(12), 7810–7823 (2020).
75. M. J. Saber and S. M. S. Sadough, "On secure free-space optical communications over Málaga turbulence channels," *IEEE Wirel. Commun. Lett.* **6**(2), 274–277 (2017).
76. Y. Ai et al., "Secure outage analysis of FSO communications over arbitrarily correlated Málaga turbulence channels," *IEEE Trans. Veh. Technol.* **70**(4), 3961–3965 (2021).
77. E. Erdogan et al., "The secrecy comparison of RF and FSO eavesdropping attacks in mixed RF-FSO relay networks," *IEEE Photonics J.* **14**(1), 1–8 (2021).
78. M. A. Amirabadi and V. T. Vakili, "A new optimization problem in FSO communication system," *IEEE Commun. Lett.* **22**(7), 1442–1445 (2018).
79. D. K. Borah and D. G. Voelz, "Pointing error effects on free-space optical communication links in the presence of atmospheric turbulence," *J. Lightwave Technol.* **27**(18), 3965–3973 (2009).
80. A. Tahami et al., "A new relay based architecture in hybrid RF/FSO system," *Phys. Commun.* **36**, 100818 (2019).
81. B. Bag et al., "Performance analysis of hybrid FSO systems using FSO/RF-FSO link adaptation," *IEEE Photonics J.* **10**(3), 7904417 (2018).
82. M. Miao and X. Li, "Novel approximate distribution of the sum of lognormal-Rician turbulence channels with pointing errors and applications in MIMO FSO links," *IEEE Photonics J.* **14**(4), 1–15 (2022).
83. F. Grosshans and P. Grangier, "Continuous variable quantum cryptography using coherent states," *Phys. Rev. Lett.* **88**(5), 057902 (2002).
84. F. Grosshans et al., "Quantum key distribution using Gaussian-modulated coherent states," *Nature* **421**(6920), 238–241 (2003).
85. F. Laudenbach et al., "Continuous-variable quantum key distribution with Gaussian modulation-the theory of practical implementations," *Adv. Quantum Technol.* **1**(1), 1800011 (2018).
86. R. Garca-Patrón and N. J. Cerf, "Continuous-variable quantum key distribution protocols over noisy channels," *Phys. Rev. Lett.* **102**(13), 130501 (2009).
87. P. Papanastasiou, C. Weedbrook, and S. Pirandola, "Continuous-variable quantum key distribution in uniform fast-fading channels," *Phys. Rev. A* **97**(3), 032311 (2018).
88. P. V. Trinh et al., "Design and security analysis of quantum key distribution protocol over free-space optics using dual-threshold direct-detection receiver," *IEEE Access* **6**, 4159–4175 (2018).
89. N. Alshaer and T. Ismail, "Performance evaluation and security analysis of UAV-based FSO/CV-QKD system employing DP-QPSK/CD," *IEEE Photonics J.* **14**(3), 21702207 (2022).
90. I. B. Djordjevic, "Hybrid QKD protocol outperforming both DV-and CV-QKD protocols," *IEEE Photonics J.* **12**(1), 1–8 (2019).
91. T. V. Nguyen, H. D. Le, and A. T. Pham, "On the design of RIS-UAV relay-assisted hybrid FSO/RF satellite-aerial-ground integrated network," *IEEE Trans. Aerosp. Electron. Syst.* **59**(2), 757–771 (2022).
92. J. Yuan et al., "A novel system of mixed RF/FSO UAV communication based on MRR and RIS by adopting hybrid modulation," *Photonics* **9**(6), 379 (2022).
93. M. T. Dabiri et al., "Modulating retroreflector based free space optical link for UAV-to-ground communications," *IEEE Trans. Wirel. Commun.* **21**(10), 8631–8645 (2022).

Aanchal Gupta is a PhD research scholar at Punjab Engineering College (Deemed to be University), Chandigarh. She received her BTech degree in electronics and communication engineering from Meerut Institute of Engineering and Technology, Meerut, (U.P), in 2009, and her MTech degree in signal processing (ECE) from Netaji Subhas Institute of Technology, Dwarka, New Delhi, in 2012. Her area of research includes optical and wireless communication.

Divya Dhawan is an associate professor in Electronics and Communication Engineering Department at Punjab Engineering College (Deemed to be University), Chandigarh. She received her PhD in the area of optical communication in 2017. Her research interests include optical OFDM, passive optical networks, digital system design, and optical sensors. She has several publications in the area of optical communication. She is a member of various technical societies, such as IEEE (electronic devices), ISTE, and IEI.

Neena Gupta is a professor in the Electronics and Communication Engineering Department at Punjab Engineering College (Deemed to be University), Chandigarh. She is a senior member of IEEE and has vast teaching and research experience. She received her BE degree in electronics and communication engineering in 1988 and her ME degree (electronics) in 1992 from Punjab University. She received her PhD from Punjab University in 2002 in the field of optical communication. Her research interests include optical communication.